



1 **Tidal influences on a future evolution of the Filchner-Ronne**  
2 **Ice Shelf cavity in the Weddell Sea, Antarctica**

3 Rachael D. Mueller<sup>1</sup>, Tore Hattermann<sup>2,3</sup>, Susan L. Howard<sup>4</sup>, Laurence Padman<sup>5</sup>,

4 <sup>1</sup>Earth & Space Research, Bellingham, WA 98225, USA

5 <sup>2</sup>Akvaplan-niva, Tromsø, 9296, Norway

6 <sup>3</sup>Alfred Wegener Institute, Helmholtz Centre for Polar and Marine Research, 27570  
7 Bremerhaven, Germany

8 <sup>4</sup>Earth & Space Research, Seattle, WA 98121, USA

9 <sup>5</sup>Earth & Space Research, Corvallis, OR 97333, USA

10 *Correspondence to:* Rachael D. Mueller ([mueller@esr.org](mailto:mueller@esr.org))

11 **Abstract.** Recent modeling studies of ocean circulation in the southern Weddell Sea,  
12 Antarctica, project an increase over this century of ocean heat into the cavity beneath  
13 Filchner-Ronne Ice Shelf (FRIS). This increase in ocean heat would lead to more basal  
14 melting and a modification of the FRIS ice draft. The corresponding change in cavity shape  
15 will affect advective pathways and the spatial distribution of tidal currents, which play  
16 important roles in basal melting under FRIS. These feedbacks between heat flux, basal  
17 melting, and tides will affect the evolution of FRIS under the influence of a changing  
18 climate. We explore these feedbacks with a three-dimensional ocean model of the southern  
19 Weddell Sea that is forced by thermodynamic exchange beneath the ice shelf and tides along  
20 the open boundaries. Our results show regionally-dependent feedbacks that, in some areas,  
21 substantially modify the melt rates near the grounding lines of buttressed ice streams that  
22 flow into FRIS. These feedbacks are introduced by variations in meltwater production as  
23 well as the circulation of this meltwater within the FRIS cavity; they are influenced locally



24 by sensitivity of tidal currents to water column thickness and non-locally by changes in  
25 circulation pathways that transport an integrated history of mixing and meltwater  
26 entrainment along flow paths. Our results highlight the importance of including explicit tidal  
27 forcing in models of future mass loss from FRIS and from the adjacent grounded ice sheet as  
28 individual ice stream grounding zones experience different responses to warming of the  
29 ocean inflow.

## 30 **1 Introduction**

31 The dominant terms in Antarctic mass budget are gains from snowfall and loss by dynamic  
32 flow of ice into the ocean. During the period of 2002-2016, the changes in snowfall were  
33 small (Monaghan et al., 2006) while mass loss from basal melting at the ice-ocean interface  
34 increased (Rignot et al., 2013; Harig and Simons, 2015), largely as a result of changes in the  
35 Amundsen Sea sector (Sutterley et al., 2014). The melting in these floating portions of the  
36 ice sheet, known as ice shelves, translates to a retreat or thinning of the grounded ice due to  
37 a reduction in back-stress (“buttressing”) that drives a dynamic acceleration of the grounded  
38 ice (e.g., Scambos et al., 2004; Dupont and Alley, 2005; Rignot et al., 2014). This  
39 acceleration of grounded ice due to ice shelf basal melting has been observed in the Pine  
40 Island, Thwaites, and other glaciers flowing into Pine Island Bay (Mouginot et al., 2014;  
41 Khazendar et al., 2016) and is responsible for the acceleration of Antarctic mass loss  
42 between 2002–2015, as demonstrated by gravity measurements taken by the GRACE  
43 satellite (Harig and Simons, 2015; Groh and Horwath, 2016). Observations (Christianson et  
44 al., 2016; Webber et al., 2017) and models (Joughin et al., 2014) show that the pace of ice  
45 mass loss will depend on changes in ice shelf buttressing, demonstrating a need for  
46 improving predictions of how the extent and thickness of ice shelves will change under  
47 future climate states.



48           The mass budget for an ice shelf is the sum of inputs from the dynamic flow of ice  
49 across the grounding line and snowfall, and losses from iceberg calving, basal melting,  
50 surface runoff and sublimation, the latter two being insignificant for most Antarctic ice  
51 shelves. Calving and melting each contribute roughly half of the total Antarctic Ice Sheet  
52 mass loss (Rignot et al., 2013; Depoorter et al., 2013), although this ratio varies substantially  
53 between ice shelves in different sectors. The ice shelves that are currently experiencing the  
54 most rapid thinning are in the Amundsen and Bellingshausen seas where relatively warm  
55 Circumpolar Deep Water (CDW) has direct access into the ice shelf cavities (Pritchard et al.,  
56 2012; Rignot et al., 2013). In contrast, the large ice shelves in other sectors that are not  
57 directly influenced by CDW inflows are closer to steady state, suggesting that the transport  
58 of ocean heat under these ice shelves has not changed significantly over the record of our  
59 observations.

60           We focus here the Filchner-Ronne Ice Shelf (FRIS) in the southern Weddell Sea  
61 (**Fig. 1**). FRIS is a large ice shelf (~430,000 km<sup>2</sup>) that accounts for 30% of the total area of  
62 Antarctic ice shelves; however, it only contributes 10% of the total ice shelf mass loss. For  
63 comparison, Pine Island Glacier accounts for 0.4% of total area of Antarctic ice shelves but  
64 contributes 7% of total ice shelf mass loss (Rignot et al., 2013). This disproportionately  
65 small melt contribution from FRIS may change in the coming century. Models suggest a  
66 large and persistent increase in ocean temperatures beneath FRIS in response to atmospheric  
67 changes in a warmer, future climate (Hellmer et al., 2012; Timmermann and Hellmer, 2013;  
68 Hellmer et al., 2017). In the modern state, most of the water entering the ocean cavity under  
69 the Filchner Ice Shelf (FIS) and the Ronne Ice Shelf (RIS) is derived from High Salinity  
70 Shelf Water (HSSW) with a temperature close to the surface freezing point of -1.9°C  
71 (Nicholls et al., 2009). Traces of modified Warm Deep Water (WDW) with temperature up  
72 to ~-1.4°C are found in Filchner Trough near the FIS ice front (Darelius et al., 2016), but do  
73 not appear to be a major heat source for melting beneath the ice shelf. In the warming



74 scenarios of Hellmer et al. (2012), however, almost the entire FRIS cavity is flooded by  
75 WDW with above-zero temperatures by the end of the 21<sup>st</sup> century, leading to basal melt  
76 rates an order of magnitude higher than present. In this warm state, the associated rapid  
77 thinning of the ice shelf would reduce the buttressing of the large marine-based grounded ice  
78 sheet surrounding FRIS (Ross et al., 2012), significantly accelerating future sea level rise  
79 (Mengel et al., 2016). Furthermore, simulations of Hellmer et al. (2017) show that the  
80 increased meltwater production will sustain the warm inflow, even if atmospheric conditions  
81 were reversed to a colder state, suggesting the existence of an irreversible tipping point once  
82 melting increases past a certain threshold.

83 This estimate of increased melt, however, assumes that cavity geometry does not  
84 change in a way that alters the access of ocean heat to the FRIS base. Studies of Larsen C  
85 Ice Shelf (Mueller et al., 2012) and Pine Island Glacier ice shelf (Schodlok et al., 2012)  
86 showed that changes to the ice shelf cavity shape can significantly alter the spatial pattern of  
87 basal melt rate, particularly in regions where tidal currents contribute substantially to the  
88 total turbulent kinetic energy near the ice base. Tides were not explicitly included in the  
89 forcing for the Hellmer et al. (2012) study; however, tidal currents play a critical role in  
90 setting the pattern of basal melt rates under FRIS (Makinson et al., 2011), which leads us to  
91 hypothesize that tides would influence changes in meltwater production from a warming  
92 ocean.

93 We explore this hypothesis using a suite of numerical model simulations that  
94 incorporate variations in tide forcing, initial temperature, and cavity geometry together with  
95 thermohaline interactions at the interface between the ocean and ice shelf. We then use these  
96 models to describe how feedbacks between ice shelf thinning and predicted tidal currents in  
97 the ice shelf cavity influence the evolution of a tide-dominated ice shelf environment under  
98 the condition of increased influx of ocean heat. Lastly, we consider the role of tides on basal  
99 mass loss near the grounding lines of each of the major ice streams supplying ice to FRIS, as



100 a guide to how individual ice stream grounding zones might respond to the projected  
101 increase in ocean heat flux to the FRIS cavity.

## 102 **Methods**

### 103 **2.1 Model overview and thermodynamic parameterization**

104 Our simulations were carried out with a version of the Regional Ocean Modeling System  
105 (ROMS 3.6; Shchepetkin and McWilliams, 2009) that has been modified to include  
106 pressure, friction, and surface fluxes of heat and salt imposed at the base of the ice shelf  
107 (Dinniman et al., 2007, 2011; McPhee et al., 2008; Mueller et al., 2012). ROMS is a  
108 hydrostatic, 3D primitive equation model with a terrain-following ( $\sigma$ -level) coordinate  
109 system and Arakawa-C staggered grid. Our model domain (**Fig. 1**) covers a portion of the  
110 southern Weddell Sea, Antarctica including FRIS. The grid spacing is 5 km with 24 vertical  
111 levels. A full description of model parameter choices and processing options is given in a  
112 supplementary document.

113 Two model geometries were used in our set of simulations, one representing the modern  
114 state (standard geometry) and the other representing a possible future state (modified  
115 geometry). Model geometry consists of a land mask (including grounded ice sheet), seabed  
116 bathymetry ( $h$ ), and ice draft ( $z_{ice}$ ). These grids are described in **Sect. 2.2**.

117 Our simulations were initialized with a homogeneous, stationary ocean that has a  
118 potential temperature of either  $\theta_{init} = -1.9^\circ\text{C}$  (“cold case”) or  $\theta_{init} = -1.4^\circ\text{C}$  (“warm case”).  
119 Initial salinity is defined as  $S_{init} = 34.65$  for all cases. The goal of the standard geometry cold  
120 case is to represent present-day temperature and salinity conditions of the primary water  
121 mass entering the ice shelf cavity (Foldvik et al., 2001; Nicholls et al., 2001, 2009), although  
122 our homogeneous representation is a greatly simplified version of realistic conditions. The  
123 warm case represents a moderate ocean warming scenario with an increase of  $0.5^\circ\text{C}$  in the



124 temperature of water being advected into the FRIS cavity. This change is much smaller than  
125 the 2°C temperature increase in the inflowing water by the end of this century predicted by  
126 Hellmer et al. (2012), but was chosen to investigate whether initial feedbacks due to melt-  
127 induced changes in cavity shape from initial warming might be positive or negative. Our  
128 idealized simulations do not include wind forcing, frazil ice, or sea-ice formation.  
129 Circulation develops through buoyancy forcing caused by thermodynamic exchange at the  
130 base of the ice shelves and, for tide-forced cases, by boundary conditions of tidal depth-  
131 integrated velocity and sea surface height. The thermodynamically-driven component of the  
132 circulation was introduced by scalar fluxes at the ice-ocean interface beneath FRIS. These  
133 fluxes are based on the 3-equation parameterization (Hellmer and Olbers, 1989; Holland and  
134 Jenkins, 1999):

$$Q_T^o = \rho_o c_{po} (\alpha_h u_* + m) \Delta T \text{ [W m}^{-2}\text{]}, \quad (1)$$

$$Q_S^o = \rho_o (\alpha_s u_* + m) \Delta S \text{ [kg m}^2 \text{ s]}, \text{ and} \quad (2)$$

$$T_b = T_f = 0.0939 - 0.057 S_b + 7.6410 \times 10^{-4} z_{ice} \text{ [}^\circ\text{C]}. \quad (3)$$

135 In eq. (1), the surface heat flux ( $Q_T^o$ ) is determined by the combined effect of thermal forcing  
136 and turbulent heat exchange. The thermal forcing is represented as  $\Delta T = (T_b - T_o)$ , where  
137  $T_b$  is the temperature at the ice-ocean interface and  $T_o$  is defined as the temperature of the  
138 ocean mixed layer. The value of  $T_b$  is assumed to be the freezing point temperature,  $T_f$ , and  
139 depends on the salinity at the ice-ocean interface,  $S_b$ , as well as the ice draft,  $z_{ice} < 0$  (Foldvik  
140 and Kvinge, 1974; Dinniman et al., 2007). For  $T_o$ , we follow a common approach of using  
141 the temperature of the surface  $\sigma$ -layer in place of mixed layer values, with the thickness of  
142 the surface  $\sigma$ -layer beneath the ice shelf cavity in our standard grid ranging from 2 to 24 m  
143 and with 72% of points between 5 and 15 m. The turbulent heat exchange at the ice-ocean  
144 interface is represented by a thermal transfer coefficient,  $\alpha_h$ , scaled by a friction velocity,  
145  $u_*$ . This turbulent heat exchange is then adjusted by a meltwater advection term,  $m$ , that



146 corrects the scalar fluxes for a computational drift that is introduced as an artifact of  
147 assumptions made in the numerical representation of the ice shelf as a material boundary  
148 (Jenkins et al., 2001). We define  $m = -\alpha_s u_* (1 - S_o/S_b)$  where  $S_b < 5$  and  $m = 0$  elsewhere.  
149 The friction velocity is also calculated from the surface quadratic stress of the upper sigma  
150 level, such that  $u_* = C_d^{1/2} |\mathbf{u}|$  with a constant drag coefficient,  $C_d = 2.5 \times 10^{-3}$ , and the  
151 magnitude of the surface layer current,  $|\mathbf{u}|$ . The potential density of seawater,  $\rho_o(x, y, z, t)$ , is  
152 evaluated for the uppermost layer, with the heat capacity of the ocean,  $c_{po}$ , given by  
153  $c_{po} = 3985 \text{ J kg}^{-1} \text{ }^\circ\text{C}^{-1}$ .  $\Delta S$  is the salinity equivalent to  $\Delta T$  and is defined as  $\Delta S = (S_b - S_o)$ ,  
154 with  $S_b$  solved by quadratic formula from combining Eq. 1, 2, and 3 (without the meltwater  
155 advection term,  $m$ ) and  $S_o$  representing the surface  $\sigma$ -layer salinity.

156 These heat and salt fluxes ( $Q_T^o, Q_S^o$ ) depend on scalar transfer coefficients ( $\alpha_h, \alpha_s$ ) that are  
157 proportional to each other by a “double diffusive” parameter,  $R = \alpha_h/\alpha_s$  (McPhee et al.,  
158 2008). Chapter 2 in Mueller (2014) provides a more detailed explanation of the background  
159 and motivation for this parameterization. Here, we used scalar transfer coefficients based on  
160 observations of the Ronne sub-ice-shelf cavity (Jenkins et al., 2010), with  $\alpha_h = 1.1 \times 10^{-2}$  and  
161  $R = 35.5$ . The meltwater-equivalent meltrate term is derived by scaling the heat flux,  $Q_o^T$ , by  
162 latent heat,  $L = 3.34 \times 10^5 \text{ J kg}^{-1}$ , and the density of ice,  $\rho_i = 918 \text{ kg m}^{-3}$ , such that

163  
164 
$$w_b = -Q_o^T L / \rho_i \text{ [m s}^{-1}\text{]}. \quad (4)$$

165  
166 Melting ice is indicated by  $w_b > 0$  and represents the thickness of freshwater added to the  
167 ocean surface, per second. These equations highlight that basal melting is driven by ocean  
168 heat and motion, the latter being influenced by thermohaline circulation and tides.

169 A set of 12 model simulations was performed and is summarized in **Table 1**. A detailed  
170 description of the different simulations is given in **Sect. 2.3**. Each case involves a



171 combination of standard or modified geometry, cold or warm ocean, and tidal forcing  
172 switched off or on. For tide-forced simulations, tide heights and barotropic currents were  
173 specified along the domain's open-ocean boundaries (see **Fig. 1**). The tidal boundary  
174 conditions were obtained for the four most energetic tidal constituents,  $K_1$ ,  $O_1$ ,  $M_2$ , and  $S_2$   
175 from the CATS2008b barotropic inverse tide model, an updated version of the circum-  
176 Antarctic model described by Padman et al. (2002). These four constituents account for 94%  
177 of the total tidal kinetic energy for this region, based on CATS2008b estimates. Flather  
178 boundary conditions were used for the barotropic velocity (Flather, 1976) with free surface  
179 conditions following Chapman (1985). Radiation conditions for baroclinic velocities are  
180 applied according to Raymond and Kuo (1984). Tracer equations are radiated across the  
181 open boundaries (Marchesiello et al., 2001) and nudged to initial conditions over a 20-day  
182 time scale.

## 183 **2.2 Geometries**

184 The grid of seabed bathymetry ( $h$ ) over the entire domain (**Fig. 2a**) was derived from the  
185 RTOPO-1 gridded dataset (Timmerman et al., 2010). The ice shelf is represented by a non-  
186 evolving, although freely floating, surface boundary based on an ice draft ( $z_{ice}$ , **Fig. 2b**) that  
187 was also derived from RTOPO-1. The land mask was adjusted around the ice rises and  
188 rumples in the southern RIS to follow the grounding line provided by Moholdt et al. (2014).  
189 Values of  $h$  and  $z_{ice}$  in regions of the ice sheet that are grounded in the RTOPO-1 mask but  
190 floating (i.e., ice shelf) in the mask obtained from the Moholdt et al. (2014) data were  
191 computed by linear interpolation and a nearest-neighbor extrapolation to ice shelf points in  
192 the original RTOPO-1 grids.

193 The ice draft and bathymetry were each smoothed to minimize errors in the baroclinic  
194 pressure gradient term that can occur with terrain-following coordinates as used in ROMS  
195 (Beckmann and Haidvogel, 1993; Haney, 1991). Our Beckman and Haidvogel number,  $rx_0$ ,



196 is less than 0.045 along both surface and bottom topographies, and our Haney number,  $rx1$ ,  
197 is less than 10 in both surface and bottom levels except for some areas along the ice shelf  
198 front, where  $rx1$  is larger and reaches a maximum value of 17.

199 Our maximum values of  $rx1$  are larger than typically recommended for ROMS. To test  
200 whether large values lead to significant circulation from resulting errors in the baroclinic  
201 pressure gradient, we ran unforced models for each of the standard and modified grids. We  
202 initialized these models with horizontally uniform temperature and salinity fields taken from  
203 an extreme stratification profile from the standard warm case. The velocities that develop in  
204 these unforced runs represent possible errors in the full simulations. We calculate grid error  
205 by comparing the currents generated by these uniformly stratified, unforced model runs to  
206 the standard warm tide-forced and modified warm tide-forced cases. From this comparison,  
207 we estimate that the maximum error in our velocity fields is 10% for the standard grid and  
208 5% for the modified grid, but these maxima are isolated to a very limited area north and  
209 northwest of Berkner Island. The relative error over most of the domain is negligible.

210 In the smoothed standard geometry, the ice draft beneath FRIS ranges from 1537 m at  
211 the deepest part of the grounding line to 11 m at the shallowest point of the ice shelf front.  
212 Small values of ice draft near the ice front are unrealistic, but are a consequence of necessary  
213 smoothing. The region of thinned ice shelf represented by these small values is a narrow  
214 band along the ice front (**Fig. 2b and 2c**). The water column thickness,  $wct = h + z_{ice}$ , ranges  
215 from 50 m (a specified minimum value, chosen for numerical stability) to 1111 m under  
216 FRIS. In the open ocean,  $wct = h$  and has a maximum value of 1914 m.

217 Using this standard geometry, we conducted simulations for both the cold and warm  
218 cases described in **Sect. 2.1**, with and without tides. The modified geometry was then  
219 created from the output from the two 20-year tide-forced simulations (see **Sect. 2.4**) of the  
220 standard cold and standard warm cases. In creating this grid, we assumed that the RIS and  
221 FIS are both in steady state under present-day conditions (Rignot et al., 2013; Depoorter et



222 al., 2013; Moholdt et al., 2014) represented by our standard cold case, and that the most  
223 accurate simulations of basal melting will be those with tidal forcing included (Makinson et  
224 al., 2011). Steady state requires that mass input from lateral ice transport across the  
225 grounding line plus snowfall onto the ice shelf is balanced by basal melting and iceberg  
226 calving that maintains a constant ice-front position. The difference in local melt between the  
227 standard warm and standard cold cases, neglecting any ice dynamical feedbacks, would then  
228 be equivalent to the rate of change in thickness of the ice shelf, provided the change in melt  
229 rate is not offset by changes in mass inputs to the ice shelf.

230 We applied the melt-rate imbalance for a period of 50 years to provide a sufficiently  
231 large change in  $z_{ice}$  to significantly alter the general circulation and tidal currents in the  
232 cavity. The resulting modified geometry thins  $z_{ice}$  by an average across the ice shelf of 30 m  
233 and a mode of .03 m. The ice shelf thickens in the below freezing, mid-shelf regions by a  
234 maximum of 14 m and thins in the above freezing, melt regions by a maximum of 453 m  
235 (**Fig. 2c and 2d**). The combined area of where the ice shelf thickens is only 0.1% of the total  
236 ice shelf area and is characterized by an average increase of 5 m. Given that the modified-  
237 case bathymetry is the same as the standard case bathymetry, these changes in  $z_{ice}$  cause a  
238 change in  $wct$  of equal magnitude. We chose to only run the modified geometry as a warm  
239 case because it is designed to represent the FRIS cavity under warm conditions. Similar to  
240 the standard geometry, we ran the modified geometry case with and without tide forcing  
241 along the open boundaries.

### 242 **2.3 Model Simulations**

243 Three types of simulations were run: (1) tide-resolving and no thermodynamic exchange; (2)  
244 simulations with ice/ocean thermodynamics, with and without tide forcing; and (3) passive  
245 dye tracer simulations to explore circulation patterns. These runs are more fully described in  
246 the following sections.



### 247 **2.3.1 Tide-resolving simulations with no thermodynamic exchange**

248 We performed two 40-day simulations with 2-hr-averaged output, one with standard  
249 geometry and the other with modified geometry, to predict tidal current speeds. These  
250 simulations (“tides-only cases”) did not include thermodynamic interactions at the ice-ocean  
251 boundary, so that the ocean remained unstratified at its initial homogeneous state. Absent  
252 stratification, the resulting currents are barotropic in nature, although some depth-  
253 dependence arises from the friction at the seabed and ice base (see, e.g., Makinson et al.,  
254 2006).

255 The spatial characteristics of time-averaged tidal currents (**Fig. 3a,b**) were calculated as  
256 the time- and depth-averaged tidal current speed  $|\mathbf{u}|_{tide}$ , given by:

257

$$258 \quad |\mathbf{u}|_{tide} = \langle \sqrt{u_b^2 + v_b^2} \rangle_t \quad [\text{m s}^{-1}], \quad (5)$$

259

260 where  $u_b(x, y, t)$  and  $v_b(x, y, t)$  are orthogonal components of modeled, depth-averaged  
261 current and  $\langle \rangle_t$  represents temporal averaging over the last  $t = 30$  days of the model run,  
262 which characterizes two cycles of the 15-day spring-neap cycles generated by the  $M_2$ ,  $S_2$ ,  $K_1$   
263 and  $O_1$  tides. The maximum tidal speed at spring tides is, typically, about  $2 \times |\mathbf{u}|_{tide}$ .

### 264 **2.3.2 Base simulations**

265 Six simulations, each 20-30 years long, were conducted with thermodynamic exchanges of  
266 heat and freshwater at the ocean/ice-shelf interface. Output for each of these simulations was  
267 averaged over 30 days. Three of these were run with tidal forcing, two standard geometry  
268 cases, one with  $\theta_{init} = -1.9^\circ\text{C}$  (cold) and one with  $\theta_{init} = -1.4^\circ\text{C}$  (warm), and one modified  
269 geometry case with  $\theta_{init} = -1.4^\circ\text{C}$  (warm). These three simulations all reached steady state  
270 solutions over 20 years, and we refer to them as: standard cold tide-forced, standard warm



271 tide-forced, and modified warm tide-forced (**Table 1**). We then used the last 30-day  
272 averaged output grids in these tide-forced solutions as initial conditions for three “restart”  
273 simulations without tidal forcing, each of which reached a new steady state over 10 model  
274 years. We refer to the individual runs as: standard cold no-tides, standard warm no-tides, and  
275 modified warm no-tides.

### 276 **2.3.3 Passive dye tracer simulations**

277 Three simulations were run with passive dye tracers to investigate the advection and  
278 diffusion of water from different regions. These simulations were initialized with the steady-  
279 state solutions of the standard cold, standard warm, and modified warm tide-forced cases.  
280 They were run for 2 years each, with 30-day averaged output. Two types of dyes were used.  
281 Passive “meltwater” dyes were continuously added to the model’s surface sigma layer at a  
282 rate of  $1 \times 10^4 w_b$  in six regions, the grounding zones of five tributary glaciers plus South  
283 Channel (**Fig. 4**). A “bulk” dye was added to the open ocean region shown in **Fig. 4**. The  
284 bulk dye was initialized at a concentration of 100%, but was not replenished after these  
285 simulations began.

## 286 **Results**

287 The main result of our study is that melt-induced changes in cavity shape introduce regional  
288 variations in tide current speeds and advection pathways that result in differing feedbacks to  
289 basal melting. We explain these insights in the following subsections through analyses of:  
290 tidal currents, spatial patterns of  $w_b$ , ice-shelf-averaged  $w_b$  and its sensitivity to model setup,  
291 regionally-averaged  $w_b$  and its sensitivity to model setup, and ocean circulation patterns  
292 shown by maps of dye tracer distribution.



## 293 2.4 Tidal currents in tide-resolving simulations

294 The maps of  $|\mathbf{u}|_{tide}$  defined by Eqn. (5) (Fig. 3a and 3b) highlight the spatial variability of  
295 tidal currents beneath FRIS. In particular, they show negligible tidal currents in the inlets of  
296 the major ice streams that feed into the RIS and FIS, and local maxima along the  
297 northeastern RIS front and the South Channel.

298 The maximum along the northeastern ice shelf frontal zone (ISFZ) of the RIS front is  
299 consistent with previous tide models (e.g., Robertson et al., 1998; Makinson and Nicholls,  
300 1999). This region has a relatively small  $wct$  (Fig. 2c), so a larger tidal current here is  
301 expected. The melt-induced geometry change in the modified case (Fig. 3c) has the overall  
302 effect of increasing the water depth in this region and reducing these tidal currents (Fig. 3d).

303 Tidal currents in South Channel are not as strong as those in the northeastern ISFZ, but  
304 the melt-induced change in  $wct$  and  $|\mathbf{u}|_{tide}$  is larger than in the ISFZ (Fig. 3c and 3d). The  
305 melt-induced change in  $wct$  is also large along the outer grounding line of FIS (Fig. 3c).  
306 These changes in  $wct$  and  $|\mathbf{u}|_{tide}$  enhance barotropic tidal transport ( $|\mathbf{u}|_{tide} \times wct$ ) along the  
307 southern edge of South Channel, the interior grounding line of FIS, and along the western  
308 edge of Berkner Island (Fig. 3e). These comparisons show that melt-induced ice shelf  
309 thinning generally reduces the local tidal currents (Figs. 3c,d). However, larger-scale  
310 reorganization of the barotropic tidal energy fluxes under FRIS also occurs (see, e.g., Rosier  
311 et al. (2014) and Padman et al. (in review), so that simple scaling of modern tidal currents by  
312 the change in  $wct$  is not possible.

## 313 2.5 Spatial pattern of melt rates ( $w_b$ ) in the base simulations

314 The six base simulations described in Sect. 2.3.2 are analyzed here to quantify the sensitivity  
315 of the spatial pattern of basal melt rates ( $w_b$ ) to  $\theta_{mit}$ , tides, and geometry.



### 316 **2.5.1 Base simulation “no-tides” cases**

317 The pattern of  $w_b$  in the standard cold no-tides case (**Fig. 5a**) is generally consistent with the  
318 increase in thermal forcing at the ice base ( $\Delta T = (T_f - T_o)$ ) due to the depression of the in  
319 situ freezing point temperature of seawater ( $T_f$ ) as pressure increases. The greatest values of  
320  $w_b$  occur along the deepest grounding lines (see **Fig. 2** for geometry), notably in the Support  
321 Force, Foundation, and Rutford inlets. This pattern of pressure-dependent melt fuels the ice  
322 pump mechanism that drives thermohaline circulation within the cavity and causes  
323 refreezing conditions ( $w_b < 0$ ) by ascending melt water to the mid-ice-shelf regions, as can  
324 be seen under the central RIS and near the RIS ice front. Since our model does not include a  
325 mechanism for frazil-ice formation, these refreezing regions represent where ice would form  
326 by direct accretion to the ice base.

327 The pattern of  $w_b$  for the standard warm no-tides case (**Fig. 5b**) is generally similar to  
328 the standard cold no-tides case (**Fig. 5a**) but with increased melt rates. Changing cavity  
329 shape while imposing the same initial ocean temperature in the modified warm case (**Fig.**  
330 **5c**) only slightly modifies melt rates for the no-tides scenario (cf. **Fig. 5b and 5c**).

### 331 **2.5.2 Base simulation “tide-forced” cases**

332 Adding tide forcing to the standard cold case changes the magnitude and pattern of  $w_b$   
333 (compare **Figs. 5a and 5d**). Melt rates increase around the grounding line and, more notably,  
334 in South Channel, where tidal currents are strong (**Fig. 5g**). The increase in  $w_b$  in South  
335 Channel between the standard no-tides and tide-forced cases exceeds  $2 \text{ m a}^{-1}$ . Adding tides  
336 also leads to an increase in refreezing in portions of the RIS, including north of Korff Ice  
337 Rise and along the coast of the northeastern RIS. This increase in refreezing with tides can  
338 be explained by the increased production of cold, buoyant meltwater from the deeper parts



339 of the ice shelf and is qualitatively consistent with the effects of adding tides reported by  
340 Makinson et al. (2011).

341 The standard warm case follows the standard cold case in that  $w_b$  increases around the  
342 deep grounding lines when tides are added (compare **Figs. 5b and 5e**). In the warm case,  
343 however, this increased melt doesn't enhance mid-shelf basal freeze conditions as much as  
344 in the standard cold case. Consequently, the increase of refreezing under the RIS is less  
345 pronounced than for the standard cold tide-forced case (compare **Fig. 5e** with **Fig. 5d**).  
346 There are two possible factors contributing to this result. First, the meltwater product at the  
347 deepest grounding lines in the warm case is warmer than in the cold case and, hence, has a  
348 smaller potential for supercooling when reaching shallower parts of the ice base. Second, the  
349 rising meltwater may warm on its ascent due to admixture of warmer ambient water in the  
350 ice shelf cavity. Both factors are consistent with an increase in thermohaline circulation in  
351 response to warmer temperatures. Similar to the standard warm tide-forced case, the  
352 modified warm tide-forced case (**Fig. 5f**) also exhibits this amplifying effect of tides on  
353 basal melt as the standard warm tide-forced case, although with regional differences when  
354 compared to the standard warm tide-forced case (compare **Figs. 5i and 5h**).

355 The differences between the tide-forced and no-tides cases for all three model setups  
356 (**Fig. 5g-5i**) show that the principal effect of tides is to increase  $w_b$  under FIS and South  
357 Channel, with South Channel exhibiting the largest change between the two.

## 358 **2.6 Sensitivity of $w_b$ to tides, $\theta_{init}$ and geometry in the base simulations**

359 We summarize the effect of  $\theta_{init}$  and geometry through values averaged over the ice shelf  
360 area. Net mass change ( $M_b$ : Gt a<sup>-1</sup>) and averaged values of  $w_b$  were calculated for three  
361 regions: (1) all of FRIS, (2) areas for which melting conditions are predicted ( $w_b > 0$ ), and  
362 (3) areas where freezing conditions are predicted ( $w_b < 0$ ). The freeze-only and melt-only



363 calculations of mass change are influenced by the mean magnitude of  $w_b$  as well as the  
364 extent of melting and freezing regions (**Fig. 5**).

365 Ocean temperature is the dominant control on integrated  $M_b$  and ice shelf averaged  $w_b$   
366 (**Fig. 6; Table 2**). Regardless of tides and geometry, warming the ocean inflow by 0.5°C  
367 increases net mass loss by a factor of ~3-5. The integrated mass gain due to freezing (marine  
368 ice accretion) is insensitive to temperature for the no-tide cases but sensitive to temperature  
369 for the tide-forced cases (**Fig. 6a**), suggesting that accurate predictions of marine ice  
370 accretion requires accurate representation of tidal currents in simulations.

371 Tides change the effect of ocean heat on  $M_b$  and  $w_b$ . In particular, the addition of tides  
372 to the standard cold case (our approximation to the modern state) increases net freezing by a  
373 factor of four, almost exactly offsetting a factor of ~2 increase in  $M_b$  in melt-only regions.  
374 For the warm cases, tides increase total mass loss in melting regions by about 20–40%, with  
375 most of this increase occurring in South Channel and under FIS (see **Fig. 5**). In contrast to  
376 the cold case, the increases in net freezing in the warm cases is small compared with the  
377 increased mass loss, so that the total basal mass loss for FRIS increases significantly when  
378 tides are added to a warm ocean. We attribute this result to production of a warmer plume  
379 near the deep grounding lines as a result of heat in the mixed layer that isn't fully utilized to  
380 fuel melting.

381 Changing geometry has a much smaller but still significant effect on ice-shelf-  
382 integrated  $M_b$  and averaged  $w_b$ . In the no-tides simulations, the change from standard to  
383 modified geometry causes net mass loss to increase slightly, suggesting a weak positive  
384 feedback, while the tide-forced cases show a slight decrease, or negative feedback (**Fig. 6**).  
385 This change in sign in the mass loss anomaly is driven primarily by the anomalous behavior  
386 of South Channel, and will be discussed in greater detail in **Sect. 3.4 and 4.3**.



## 387 **2.7 Regional sensitivity of $w_b$ in the base simulations**

388 Regional averages of  $w_b$  (**Fig. 7**) indicate that basal mass loss near grounding lines of major  
389 inflowing ice streams varies by an order of magnitude within a given simulation. Support  
390 Force, Foundation and Rutford ice streams show the largest values, exceeding  $2 \text{ m a}^{-1}$  for the  
391 standard cold cases with and without tide forcing. In contrast, modeled melt rates for Möller  
392 and Institute ice streams are in the range of  $0.28\text{--}0.44 \text{ m a}^{-1}$  for the standard cold case runs.

393 For each ice stream inlet,  $\theta_{init}$  is the primary control on melt rate near the grounding line,  
394 with mean melt rate approximately doubling from the standard cold case to the standard  
395 warm case. Tidal forcing is a secondary control that leads to either an increase or decrease in  
396  $w_b$  near grounding lines. For Foundation and Rutford ice streams, adding tides reduces area-  
397 averaged melt rates, with the relative change being larger for the warm cases with both  
398 standard and modified geometry. The largest fractional change in melt rate due to tides  
399 occurs near the Rutford Ice Stream grounding line in the modified-geometry warm case,  
400 where adding tides reduces mean melt rate by 40% from  $7.7 \text{ m a}^{-1}$  to  $4.6 \text{ m a}^{-1}$ .

401 South Channel is an exception to the general result that regional sensitivity of  $w_b$  is  
402 more strongly affected by changes in  $\theta_{init}$  than tidal forcing. In this region,  $w_b$  increases by  
403 roughly an order of magnitude between the no-tide and tide-forced simulations, whereas the  
404 fractional change due to  $\theta_{init}$  is much smaller, about a factor of  $\sim 2$  (**Fig. 7**). South Channel  
405 also experiences a large reduction ( $\sim 30\%$ ) in regionally-averaged  $w_b$  in the modified warm  
406 tide-forced run compared with the standard warm tide-forced run. We attribute this change  
407 in  $w_b$  to the reduction in tidal currents as geometry is changed (**Fig. 3**).

## 408 **2.8 Ocean circulation within the FRIS cavity in the passive-dye tracer simulations**

409 General patterns of water mass circulation into and under FRIS are demonstrated by output  
410 from the two-year simulations with passive-tracer dyes (see **Sect. 2.3.3**). We focus only on



411 tide-forced simulations because, as discussed in **Sect. 3.4** and described by Makinson et al.  
412 (2011), tidal currents are known to be critical to patterns of basal melting beneath FRIS.

### 413 **2.8.1 Dye tracer circulation in standard cold tide-forced case**

414 The concentration of the open ocean bulk dye tracer in the upper  $\sigma$ -layer (**Fig 8a**) reveals  
415 that the FRIS cavity has two different sources of heat inflow. The FIS and innermost RIS  
416 cavities are flooded by a southward transport of the open continental shelf waters across the  
417 FIS ice front, whereas the cavity circulation in the northeastern portion of RIS is dominated  
418 by incursions of water from across the RIS front. The latter inflow does not penetrate deep  
419 into the central and southern RIS within two years of simulation, although this is likely to be  
420 an artefact of the omission of the high salinity shelf water that is known to be formed at the  
421 RIS front and is assumed to fuel gravity currents that reach the deep western grounding lines  
422 of the RIS. In our simulations, the water entering through FIS circulates clockwise along the  
423 deep grounding line. After two years, some dye has reached as far west as Carlson inlet;  
424 however, very little of this dye is found under the central RIS north of the ice rises and  
425 rumples. Support Force, Foundation, and South Channel are most directly impacted by open  
426 ocean inflow. This circulation is generally consistent with the progression of ocean warming  
427 in the Hellmer et al. (2012) model.

428 Meltwater produced near Foundation Ice Stream grounding line (**Fig. 8b**) reveals  
429 similar clockwise circulation. This water reaches the western RIS ice front in about two  
430 years. Meltwater from Foundation inlet flows into all ice stream inlets to the west of  
431 Foundation. The flow of this meltwater through South Channel is limited to the southern  
432 side of the channel.

433 Meltwater produced in South Channel also reaches all of the western RIS within two  
434 years (**Fig. 8c**), including much of the central region where refreezing occurs. Meltwater  
435 produced in Rutford inlet flows northward to the west of Korff Ice Rise (**Fig. 8d**).



436        These dye maps demonstrate that water found in the uppermost layer, in contact with  
437        the ice shelf base, in a specific ice stream inlet is a mixture of the incoming high-salinity  
438        ocean water and meltwater that was produced at other inlets further upstream. As an  
439        important consequence, changes in meltwater production in different regions will alter the  
440        meltwater plume characteristics (e.g., temperature) experienced by downstream ice stream  
441        grounding zones. In the following, it will be shown that these interaction of different  
442        grounding zones leads to non-local feedbacks of the melting response to changes in ocean  
443        temperatures and ice shelf geometry, for modeling of which an explicit inclusion of tidal  
444        currents is one of the key ingredients.

#### 445    **2.8.2    FRIS cavity dye tracer distribution for tide-forced cases**

446        Comparisons of dye concentration maps after two years of integration for the three tide-  
447        forced simulations (**Fig. 9**) show differences that can be attributed both to  $\theta_{mit}$  (comparing  
448        standard cold and standard warm cases) and to geometry (comparing standard warm and  
449        modified warm cases).

450        The stronger cavity circulation introduced by the amplification of net basal melting for  
451        the warmer ocean,  $\theta_{mit} = -1.4^{\circ}\text{C}$ , increases inflow through the FIS and into the RIS cavity  
452        (upper row of **Fig. 9**). Open-ocean water is present under most of RIS after two years in the  
453        standard warm case. The dye concentration of open-ocean water under the northern portion  
454        of RIS decreases as  $\theta_{mit}$  increases, indicating that the stronger northward flow of meltwater  
455        in the warm case reduces the contribution of the direct open-ocean inflow to the northern  
456        RIS. This influence of  $\theta_{mit}$  on strengthening the sub-ice-shelf cavity circulation decreases  
457        slightly in the modified warm case, which shows less open water dye penetrating into the  
458        innermost RIS than the standard warm case solution (compare the two upper right subplots  
459        of **Fig. 9**).



460 Comparisons of meltwater dyes from ice stream inlets and South Channel (lower six  
461 rows in **Fig. 9**) show, in all cases, more rapid ventilation of downstream regions when  $\theta_{init}$  is  
462 warmer. In these simulations, meltwater dyes are injected continuously at a rate that is  
463 scaled to the basal melt rate (**Sect. 2.3.3**). Relative dye concentrations at specific locations  
464 can, therefore, be interpreted as the relative values of meltwater from different sources with  
465 total meltwater plume concentration being an integration of the contributions from all  
466 upstream source. Changes in the different runs reflect the response of the cavity circulation  
467 and changes in meltwater production rate in the respective grounding zones. Meltwater from  
468 South Channel dominates the central RIS, although melting in Foundation and Rutford inlets  
469 provides a substantial freshwater flux to the western RIS.

470 The changes in upper-ocean circulation caused by changes in geometry, seen by  
471 comparing the two warm cases in the last two columns of **Fig. 9**, are less obvious than the  
472 effect of changing temperature. Nevertheless, changing geometry has a significant regional  
473 effect. Foundation inlet meltwater spreads out more in the modified warm case than in the  
474 standard warm case as a result of increased dye transport through the channel between  
475 Henry Ice Rise and Berkner Island. South Channel meltwater concentrations are reduced in  
476 the modified warm case, which is consistent with the reduced melt rates in the region  
477 (**Fig. 5**). Similar to South Channel, Rutford inlet meltwater in the surface layer is also  
478 reduced for the modified geometry case.

### 479 **2.8.3 Regional meltwater dye comparison, for tide-forced cases**

480 Regional meltwater dye production and advection is evaluated from the surface levels of  
481 Foundation, Möller, and South Channel inlet regions (as in **Fig. 4**). **Fig. 10** shows the  
482 integrated values over these regions for the standard cold, standard warm and modified  
483 warm tide-forced cases. As described in **Sect 2.3.3**, meltwater dye from a particular region is  
484 a scaled quantity of  $w_b$  that reflects the magnitude of meltwater produced in that region. The



485 resulting passive dye tracer is then transported through the domain through a combination of  
486 advection and mixing and acts as a proxy for the meltwater plume. In this section, we use the  
487 quantity of these meltwater tracers to demonstrate how meltwater circulation is affected by  
488 changes in  $\theta_{init}$  and geometry.

489 Foundation inlet shows an expected increase in integrated meltwater dye with the 0.5°C  
490 increase in  $\theta_{init}$  between the standard cold and standard warm cases (**Fig. 10a**). This increase  
491 in integrated meltwater dye is not sustained with the change in cavity geometry. Instead, the  
492 net amount of dye is reduced in the modified warm case such that the value of integrated dye  
493 in the surface level more closely matches that of the standard cold case. This reduction in  
494 integrated meltwater dye between the standard warm and modified warm case carries  
495 forward into the Möller region, where the reduction of Foundation dye between the two  
496 cases is even greater than in Foundation (compare **Fig. 10a** and **10b**). At the same time, the  
497 reduction in Foundation dye in the Möller region is somewhat compensated by the Möller  
498 meltwater dye, which is consistent between the two warm cases (**Fig. 10b**). Overall, the  
499 Möller region appears to be less affected by the change in geometry than the Foundation  
500 region. Within the South Channel, the influence of geometry on the quantity of meltwater  
501 dye is compensated by changes in circulation that allow for more Foundation dye in the  
502 surface level of South Channel in the modified warm case than the standard warm case (**Fig.**  
503 **10c**). This increase in surface level Foundation dye in South Channel is caused by changes  
504 in circulation that distribute the dye more evenly across South Channel in the modified  
505 warm case than in the standard warm case (**Fig. 9**).

506 These results highlight that the regional sensitivities of meltwater dye to  $\theta_{init}$  and  
507 geometry may influence but not necessarily determine the quantity and quality of meltwater  
508 in downstream regions. This result is important because it reveals the degree to which  $\theta_{init}$   
509 and cavity shape precondition the quantity and origin of meltwater in any given region. For  
510 example, the FRIS-integrated surface dye quantity (**Fig. 10d**) for Foundation and Support



511 Force is equivalent between the standard warm and modified warm cases, even though there  
512 are strong regional variations in these cases (**Fig. 10 a-c**). In addition, the FRIS-integrated  
513 values of meltwater dyes from the ice front regions (RIS west, RIS east, and FIS) are similar  
514 among all cases while they differ among regions, showing greater amounts of dye in  
515 Foundation, Möller, and South Channel regions for the warm cases than in the cold case.  
516 These regional and integrated changes demonstrate that the FRIS meltwater product is a  
517 result of regional feedbacks that are affected by a combination of production, mixing, and  
518 advection.

## 519 **Discussion**

### 520 **2.9 Comparison of modeled, ice shelf averaged basal melt estimates with observations**

521 The melt rate averaged over the area of an ice shelf is a common metric for evaluating ice  
522 shelf mass balance (e.g., Rignot et al., 2013; Depoorter et al., 2013). Our estimate of melt  
523 rate averaged over FRIS for the standard case is  $0.14 \text{ m a}^{-1}$ , equivalent to  $\sim 48 \text{ Gt a}^{-1}$  of net  
524 mass loss (**Fig. 6** and **Table 2**). The range of values reported by other studies extends from  
525 the lower bound in Depoorter et al. (2013) of  $0.03 \text{ m a}^{-1}$  to  $0.55 \text{ m a}^{-1}$  for the first  
526 oceanographically-derived estimates reported by Jenkins (1991) and Jacobs et al. (1992); see  
527 **Fig. 11** and **Table 3**. Compared with the three most recent satellite-constrained estimates,  
528 our value is near the central estimate of  $0.12 \text{ m a}^{-1}$  of Depoorter et al. (2013), and near the  
529 lower limit of the ranges reported by Rignot et al. (2013) and Moholdt et al. (2014).

530 The range in estimates of  $w_b$  is a result of variations in observation type and model  
531 choices. Estimating  $w_b$  from observations typically requires averaging other ice shelf mass  
532 budget terms, derived from satellite observations and atmospheric models, over several  
533 years. Estimates from models are affected by model setup. Our idealized model lacks the  
534 seasonal warming of the upper ocean near the ice front that leads to significant summer



535 melting and rapid basal melting of the ice shelf frontal zone (e.g., Makinson and Nicholls,  
536 1999; Joughin and Padman, 2003; Moholdt et al., 2014). The reduced melt in the frontal  
537 zones in our model helps to explain why our ice-shelf-integrated mass loss by melting is  
538 smaller than in most observations. The lack of an annual cycle of forcing in our model might  
539 also affect our representation of inflows across the ice front. For example, high-salinity shelf  
540 water (HSSW) inflow across the western Ronne ice front is believed to be modulated not  
541 only by the annual cycle of HSSW production in the Ronne Depression but also by seasonal  
542 changes in the vorticity constraint at the ice front, associated with changing stratification  
543 (Nicholls et al., 2009). Neither of these seasonally-varying processes is included in our  
544 simulations.

#### 545 **2.10 Sensitivity of $w_b$ to $\Delta T$ and surface currents**

546 In this section, we explore the regional variations of thermal forcing ( $\Delta T$ ) and turbulent  
547 exchange on  $w_b$  using the values from the 30-day averaged output of each simulation to  
548 calculate  $\Delta T$  and  $|\mathbf{u}|$ . Note that  $w_b$  in the 30-day averaged model output is based on the  
549 average of instantaneous heat fluxes and, therefore, includes the model's knowledge of  
550 covariances between  $\Delta T$  and  $|\mathbf{u}|$  on much shorter time scales than  $|\mathbf{u}|$ , which is based on 30-  
551 day averaged u- and v-velocities. We use a linear combination of non-tidal and tidal  
552 currents,  $\mathbf{U}$ , given by

$$553 \mathbf{U} = |\mathbf{u}|_{\text{tide}} + |\mathbf{u}| \text{ [m s}^{-1}\text{]} \quad (6)$$

554 to represent the local forcing for turbulent exchange, where  $|\mathbf{u}|_{\text{tide}}$  is from **Eqn. (5)** and  $|\mathbf{u}|$   
555 is calculated from the 30-day averaged output values of u- and v-velocities. For the no-tides  
556 cases,  $|\mathbf{u}|_{\text{tide}}$  is zero and  $\mathbf{U}_{\text{no tides}} = |\mathbf{u}|$ . We include  $|\mathbf{u}|_{\text{tide}}$  in the tide-forced cases to more  
557 closely approximate the non-time-averaged relationship described by **Eqn. (1)**, because the  
558 30-day average removes the tidal signal in  $\Delta T$  and  $|\mathbf{u}|$  in the tide-forced cases.



559 Comparisons of the six base simulations show that  $w_b$  generally follows the expected  
560 functional dependence on  $\Delta T$  and  $U$  (**Fig. 12a**): in all six cases, values of  $w_b$  increase with  
561 stronger currents and more thermal forcing, with values roughly falling along lines of  
562 constant  $\Delta T \cdot U$ . However, regional differences can be seen in the bivariate relationships  
563 between  $w_b$  and either  $\Delta T$  or  $U$  (**Fig. 12b and 12c**). Most ice-stream inlet averages show a  
564 similar increase in  $w_b$  with respect to  $\Delta T$  (**Fig. 12b**), suggesting that reasonable estimates of  
565 melt rate in the ice-stream inlets could be obtained from variability of  $\Delta T$  and a constant,  
566 assumed low, value of  $U$ . South Channel and, to some degree, Institute diverge from this  
567 relationship, demonstrating a larger variability in  $w_b$  in relation to  $\Delta T$  than is seen in other  
568 inlets (**Fig. 12b**). This larger variability in  $w_b$  in South Channel arises because changes in  
569 modeled melt in this area are controlled primarily by changes in  $U$  (**Fig. 12b**).

570 Comparisons of the ratios for  $\Delta T$ ,  $U$ , and  $w_b$  at each site between simulations without  
571 and with tides (**Fig. 12d-f**) show how each region responds to the combined effects of tide-  
572 induced changes in ocean conditions. With the exception of South Channel, adding tides  
573 always cools (decreases  $\Delta T$ ) the upper layer of ocean water adjacent to the ice base (**Fig.**  
574 **12d**). On average, the largest reductions occur for the RIS ice stream inlets. We attribute this  
575 result to cooling of water entering the RIS inlets by inclusion of meltwater from upstream  
576 freshwater sources, with RIS inlets being influenced by rapid melting in Support Force and  
577 Foundation inlets, and in South Channel (**Figs. 8 and 9**).

578 The differences between the tide-forced and no-tide cases show up more strongly in the  
579 regionally-averaged comparison of  $U$  (**Eqn. (6), Fig. 12e**). In all regions, the effect of adding  
580 tides is greater for the cold standard cases than for warm standard cases. Since the value of  
581  $|\mathbf{u}|_{\text{tide}}$  in **Eqn. (5)** is the same for the standard geometry runs, this difference represents the  
582 increase in the thermohaline-driven  $|\mathbf{u}|$  from the cold to warm cases.

583 The largest differences in  $|\mathbf{u}|$  amongst all three model runs are in Möller, South Channel,  
584 and Institute inlets. For the warm cases, modifying the geometry increases the ratio of  $U_{\text{tide}}$ -



585 forced /  $U_{\text{no tides}}$  for these three regions even though tidal currents decrease (**Fig. 3**) as  $wct$   
586 increases. This response implies that  $U_{\text{no tides}}$  also declines in the modified geometry case. A  
587 decline in  $U_{\text{no tides}}$  in the modified geometry is consistent with a reduction in  $z_{ice}$  in the inlet  
588 regions, which would reduce the thermal forcing and, hence, reducing the ice pump  
589 circulation. If true, this feedback is an artifact of our model geometry, which excludes the  
590 possibility of deeper ice that could be exposed when the grounding line migrates due to the  
591 imposed thinning. Corollary evidence for this reduction in ice pump circulation is seen in the  
592 top row of **Fig. 9**.

593 The role of South Channel melt on cooling downstream ice stream inlets, its sensitivity  
594 to tides, and tidal sensitivity to changing  $z_{ice}$  suggest that reliable predictions of change in  
595 modeled  $w_b$  in the southern RIS ice streams for future climate scenarios depends on the  
596 correct representation of changes to South Channel geometry.

### 597 **2.11 Role of advection through South Channel**

598 As the maps of surface-layer dye tracers (**Fig. 8 and 9**) show, most water entering the FRIS  
599 cavity in our simulations flows southward under the FIS front and then circulates clockwise  
600 around the FIS and RIS grounding lines. A water parcel takes about two years to travel from  
601 the FIS front to the southwestern RIS region of Rutford inlet. During that time, each water  
602 parcel is subjected to mixing with meltwater, so that the properties of water entering each  
603 inlet depend on the processes along the entire inflow path. This circulation is driven only by  
604 thermohaline circulation modified by tides; recall that our model excludes the influences of  
605 wind-driven circulation and sea-ice formation.

606 Distribution of dyes also varies in the vertical, shown in **Fig. 13** for a transect taken  
607 across South Channel from the western tip of Henry Ice Rise. The standard geometry  
608 simulations show a core of open water dye along the bottom and northeastern slope of the  
609 trough. Support Force dye is concentrated near the ice base, toward the southwestern end of



610 the transect. Foundation dye appears in both the surface and deep model layers, concentrated  
611 on the southern side of South Channel (see, also, **Fig. 8b**). As expected, South Channel dye  
612 has the highest concentration in the surface waters of this transect.

613 The spatial pattern in dye distribution is fairly consistent between the warm and cold  
614 standard geometry cases, although much more open water dye from north of the ice front is  
615 present in the warm case. This quantitative difference is consistent with the overall  
616 understanding that warmer  $\theta_{ini}$  drives a stronger thermohaline circulation that enhances  
617 cavity circulation and leads to a shorter residence time (**Fig. 9**).

618 More qualitative differences between simulations arise from the change in cavity shape.  
619 Except for South Channel dye, the modified geometry shows more laterally uniform dye  
620 concentrations across the channel. Dye distribution remains vertically stratified in all three  
621 cases with the depth of the upper layer being similar in the standard warm and modified  
622 warm cases. However, even though the averaged  $w_b$  in South Channel is similar between the  
623 standard cold and modified warm cases (**Fig. 7**), the South Channel meltwater product does  
624 not mix down as far in the modified warm case as it does in the standard cold case (**Fig. 13**),  
625 which we attribute to the much weaker tidal currents in this region (**Fig. 3**) for modified  
626 geometry.

627 Transects for dye tracers are only provided for the tide-forced cases. However, a  
628 comparison of temperature transects for the no-tides and tide-forced cases (**Fig. 13**) show  
629 that the thermocline is deeper in the standard geometry tide-forced cases, with the  
630 thermocline most affected in the standard cold case. As shown in **Fig. 12d**, tides increase the  
631 thermal forcing in South Channel in the standard geometry by a factor of  $\sim 3$  while having a  
632 negligible effect on  $\Delta T$  in the modified geometry. These results suggest that the lowered  
633 thermocline in this region is caused by tide-induced mixing rather than advection, and in  
634 turn directly responds to the reduced tidal currents in the modified warm case.



## 635 2.12 Implications of regional melt on ice sheet mass balance

636 Walker et al. (2008) showed that the spatial distribution of ice shelf melt rates was critical to  
637 the behavior of the buttressed grounded-ice streams; for the same integrated mass loss from  
638 an ice shelf, grounded-ice loss was significantly faster when the melting was concentrated  
639 near the grounding line. Gagliardini et al. (2010) confirmed this analysis, and also noted that  
640 a grounded-ice stream could thicken, and its grounding line could advance even when net  
641 melting increased, if the melt rate decreased near the grounding line. In the context of our  
642 study the implication is that, even when the change in the ice shelf, area-averaged melt rate  
643 is not large, substantial variability in melt rates near ice-stream grounding lines could still  
644 have a large impact on loss of grounded ice.

645 In addition to being affected by the spatial distribution of  $w_b$ , dynamic mass loss of  
646 grounded ice is also affected by bedrock slope and ice sheet topography. These factors  
647 introduce additional spatial heterogeneity in the influence of basal melting on overall mass  
648 loss from the grounded ice streams flowing into FRIS. Wright et al. (2014) used the  
649 BISICLES ice sheet model to test the sensitivity of the grounded ice sheet to changes in  
650 FRIS mass loss at the grounding line. They found that Institute and Möller ice streams are  
651 the most sensitive to changes in basal mass balance that might be caused by a warming  
652 ocean inflow. This result was confirmed by Martin et al. (2015) using the Parallel Ice Sheet  
653 Model (PISM). These two ice streams rest on top of steep reverse bed slopes with low basal  
654 roughness, conditions which have been shown to contribute to grounding line instability and  
655 retreat (Schoof, 2007). Furthermore, these ice streams are also sensitive to changes in the  
656 buttressing effect from ice shelf mass loss around Henry and Korff ice rises and an increase  
657 in basal sliding over these ice rises. Our results indicate that tides currently exert a strong  
658 influence on basal mass balance in the area around Henry and Korff ice rises (**Fig. 5**), by  
659 increasing melting in South Channel and increasing marine ice accretion north of the ice  
660 rises and Doake Ice Rumples.



661 Möller and Institute are among the lowest meltwater producing regions (**Fig. 7**) and  
662 receive the largest fraction of meltwater product from Foundation inlet basal melt (**Fig. 10**).  
663 The relative quantities of these meltwater products are sensitive to changes in advection and  
664 mixing imposed by changes in  $\theta_{init}$  and geometry (**Sec. 3.5**). As shown in **Fig. 7**, the 0.5°C  
665 increase in  $\theta_{init}$  increases the Möller grounding-line region  $w_b$  to 1.03 m a<sup>-1</sup> (an increase of  
666 134%) and Institute grounding-line region  $w_b$  to 1.30 m a<sup>-1</sup> (an increase of 100%), for the  
667 tide-forced cases. The grounding lines in these regions appear to be very sensitive to changes  
668 in  $\theta_{init}$  and less sensitive to changes in the cavity ocean circulation imposed by a change in  
669 model geometry. Even with Möller and Institute's sensitivity to  $\theta_{init}$ , however, these inlets  
670 are buffered from variations in open ocean heat due to the combined influence of circulation  
671 pathways and inflowing meltwater derivatives (**Fig. 10**).

672 Of the nine grounding-line regions explored in this study, Foundation inlet has the  
673 highest averaged melt rate of 2.76 m a<sup>-1</sup> for the standard cold case (**Fig. 7**), a rate which  
674 more than doubles to 6.01 m a<sup>-1</sup> when  $\theta_{init}$  increases from -1.9°C to -1.4°C. However,  
675 grounded-ice mass flux from Foundation Ice Stream is less sensitive to changes in basal  
676 melting than Möller and Institute (Wright et al., 2014). According to the results presented in  
677 Wright et al. (2014), even the higher melt rate with the warmed ocean in our study is  
678 insufficient to drive grounding line retreat and significant acceleration of grounded-ice loss  
679 at Foundation. Therefore, it is possible that the dominant effect on the grounded-ice mass  
680 budget of large  $w_b$  at Foundation is through the effect of Foundation inlet meltwater on  
681 downstream inlets, particularly Möller. As shown in the dye results presented in **Sect. 3.5**,  
682 Möller is somewhat isolated from FIS inflow but flooded by Foundation meltwater.



683 **Conclusion**

684 The idealized modeling results presented here on the basal melting of FRIS, combined with  
685 ice-sheet model results reported by Wright et al. (2014), indicate that the response of the  
686 Antarctic Ice Sheet in the Weddell Sea sector to large-scale ocean warming in the Southern  
687 Ocean depends on several regional and local processes that combine to determine ocean  
688 state in individual ice-stream inlets. These processes include the tidal contribution to ocean  
689 mixing, advection of meltwater products into downstream inlets, and feedbacks between  
690 advection, tides and melting as ice shelf draft evolves.

691 In general, tides increase the area-integrated mass loss from the entire FRIS, consistent  
692 with the findings of Makinson et al. (2011); however, for our cold case ocean representing  
693 the modern state, increased basal melting with tides is completely offset by a factor-of-four  
694 increase in basal accretion (marine ice formation) in the central Ronne Ice Shelf.

695 As proposed by Hellmer et al. (2012), warming of water entering the cavity under FRIS,  
696 primarily as an inflow under the FIS front, leads to a large increase in ice-shelf-integrated  
697 mass loss. In our simulations, warming of 0.5°C increased total FRIS mass loss by a factor  
698 of ~3.6 for the no-tides simulations (cf. Hellmer et al., 2012) and by a factor of ~5.1 when  
699 tidal forcing was included.

700 The large-scale, sub-ice-shelf circulation in our idealized model is dominated by a  
701 southward inflow of open-ocean water across the Filchner Ice Shelf front, and clockwise  
702 circulation of this water along the southern grounding line. A water parcel takes about two  
703 years to travel from the Filchner ice front to the southwestern Ronne Ice Shelf. The known,  
704 seasonally varying inflow through the Ronne Depression is not represented in our model,  
705 which lacks the forcing required to drive a seasonal cycle of high salinity shelf water  
706 production and stratification along the Ronne ice front.



707 At the regional scale, complex feedbacks occur between local processes such as tide-  
708 induced mixing and advection, so that the temperature of a water parcel represents the  
709 upstream integrated history of mixing between the inflowing source water and basal  
710 meltwater. The temperature of the upper ocean layer adjacent to the ice shelf base is cooler  
711 when tide forcing is included, especially in the southern Ronne ice stream inlets (Rutford,  
712 Carlson and Evans). We attribute this cooling to incorporation of meltwater from upstream  
713 sources, notably Foundation inlet and South Channel.

714 These results show regionally variable responses to changes in tides,  $\theta_{mit}$ , and cavity  
715 geometry that can be summarized as follows.

- 716 (1) Meltwater plumes from basal melting introduce non-local feedbacks, within the  
717 same cavity, in response to variations of inflowing ocean heat and melt-induced  
718 changes in ice draft.
- 719 (2) Tides increase  $w_b$  under the FIS, with largest effect within South Channel.
- 720 (3) In some regions (e.g. South Channel), tides influence  $w_b$  directly by changing  
721 the friction velocity; in other regions (e.g., Rutford), tides influence meltwater  
722 production through changes in  $\theta$  by mixing along the upstream flow path. Tides  
723 affect how  $w_b$  changes in response to  $\theta_{mit}$  and cavity geometry by these direct  
724 and indirect influences.
- 725 (4) The greatest fraction of meltwater in the Möller and Institute inlets are  
726 contributed by Foundation inlet.

727 The described regional meltwater distribution and  $w_b$  is sensitive to the accuracy of our  
728 grids of seabed depth and  $wct$ , which are based on few passive seismic measurements in  
729 regions of strong model sensitivity (**Fig. 3f**). Distributions are also affected by the model  
730 configuration, including neglect of atmospheric and sea-ice forcing, the choice of mixing  
731 schemes and the thermodynamic exchange coefficients for the ice-ocean boundary layer



732 parameterization. However, our analysis shows that the interplay of tides, far-field thermal  
733 forcing and the oceanic response to ice shelf geometry changes leads to complex and  
734 sometimes non-local interactions that alter the overall basal mass balance that effects  
735 melting near the grounding lines, thereby controlling the dynamical response of adjacent  
736 grounded ice streams.

737 A significant source of uncertainty in the future mass loss through the ice streams  
738 draining the West Antarctic Ice Sheet into the Ronne Ice Shelf is in how the ice draft in  
739 South Channel will evolve if the heat flux into the cavity under FRIS increases. Under  
740 modern conditions and with the seabed and ice draft represented by the RTOPO-1 database,  
741 tides are a critical contributor to basal melting in the region. A warmer ocean will increase  
742 mass loss by basal melting that will lead to ice shelf thinning unless it is offset by increased  
743 inputs from ice advection and snowfall. However, this thinning then causes regional  
744 feedbacks that include a reduction in basal melting in South Channel, as tidal currents  
745 weaken, and a change in circulation pathways with consequences for heat and meltwater  
746 transport.

747 We conclude that it is not possible to predict the true effect of oceanic warming on ice  
748 thinning near individual ice stream grounding lines without a better understanding of the  
749 feedbacks introduced by tidal forcing and circulation as a result of changes in *wct*. That is, as  
750 coupled ocean/ice-sheet models become a standard tool for projecting ice sheet response to  
751 changing climate, tides must be either explicitly modeled, or represented by a  
752 parameterization that itself can evolve with time at a rate set by the evolution of the cavity.  
753 Furthermore, potential bottlenecks in sub-ice-shelf circulation of ocean heat must be  
754 identified through improved surveys of seabed bathymetry which, when combined with the  
755 better-known ice shelf draft, determines both the tidal current speeds and the mean ocean  
756 circulation towards downstream sites including ice-stream inlets. While FRIS is presently in



757 approximate steady state, the potential for future ocean warming, increased  $w_b$ , and a  
758 corresponding mass loss causing a ~1 m sea-level rise supports the need to improved  
759 measurements of the seabed bathymetry in the ice stream inlets and under South Channel.

#### 760 **Author contribution**

761 R.D.M. led the study. The simulations were designed by R.D.M. and L.P., implemented by  
762 R.D.M. and S.L.H., and analyzed by R.D.M., L.P. and T.H. The paper was written  
763 by R.D.M., L.P. and T.H.

#### 764 **Acknowledgements**

765 We thank Mike Dinniman (Old Dominion University) for his invaluable help in developing  
766 ROMS for use in simulating ice shelves and Dr. Scott Springer for his help in creating the  
767 model grid. This study was funded by: NASA grants NNX10AG19G, NNX13AP60G;  
768 NASA Earth and Space Science Fellowship, 07-Earth07F-0095; and The Research Council  
769 of Norway, program FRINATEK, project WARM #231549/F20. This is ESR publication  
770 number XXX.

#### 771 **References**

772 Arzeno, I. B., Beardsley, R. C., Limeburner, R., Owens, B., Padman, L., Springer, S. R.,  
773 Stewart, C. L., and Williams, M. J. M.: Ocean variability contributing to basal melt rate  
774 near the ice front of Ross Ice Shelf, Antarctica, *J. Geophys. Res. Oceans*, 119, 4214–  
775 4233, doi:10.1002/2014JC009792, 2014.



- 776 Beckmann, A. and Haidvogel, D.B.: Numerical simulation of flow around a tall isolated  
777 seamount. Part 1: Problem formulation and model accuracy, *J. Phys. Oceanogr.*, **23**,  
778 1736–1753, 1993.
- 779 Chapman, D.: Numerical treatment of cross-shelf open boundaries in a barotropic coastal  
780 ocean model, *J. Phys. Oceanogr.*, **19**, 384–391, 1985.
- 781 Christianson, K., Bushuk, M., Dutrieux, P., Parizek, B.R., Joughin, I.R., Alley, R.B., Shean,  
782 D.E., Abrahamsen, E.P., Anandakrishnan, S., Heywood, K.J., Kim, T.W.: Sensitivity of  
783 Pine Island Glacier to observed ocean forcing. *Geophys. Res. Lett.* **43**, 10817–10825,  
784 doi: 10.1002/2016GL070500, 2016.
- 785 Darelus, E., Fer, I., and Nicholls, K. W.: Observed vulnerability of Filchner-Ronne Ice  
786 Shelf to wind-driven inflow of warm deep water. *Nature Comms.*, **7**, 2016.
- 787 Dinniman, M. S., Klinck, J. M., and Smith Jr., W. O.: Influence of sea ice cover and icebergs  
788 on circulation and water mass formation in a numerical circulation model of the Ross  
789 Sea, Antarctica. *J. Geophys. Res.*, **112**, C11013, doi:10.1029/2006JC004036, 2007.
- 790 Dinniman, M. S., Klinck, J. M. , and Smith, Jr., W. O.: A model study of Circumpolar Deep  
791 Water on the West Antarctic Peninsula and Ross Sea continental shelves, *Deep-Sea Res.*  
792 **II.**, **58**, 1508–1523, doi:10.1016/j.dsr2.2010.11.013, 2011.
- 793 Depoorter, M., Bamber, J. , Griggs, J. , Lenaerts, J. , Ligtenberg, S. , van den Broeke, M.,  
794 and Moholdt, G.: Calving fluxes and basal melt rates of Antarctic ice shelves, *Nature*,  
795 **502**, 89–92, doi:doi:10.1038/nature12567, 2013.
- 796 Dupont, T. K. and Alley, R. B.: Assessment of the importance of ice-shelf buttressing to ice-  
797 sheet flow. *Geophys. Res. Lett.* **32**, L04503, 2005.
- 798 Flather, R.: A tidal model of the northwest European continental shelf, *Memoires de la*  
799 *Société Royale des Sciences de Liège*, **6**, 141–164, 1976.
- 800 Foldvik, A., and Kvinge, T.: Conditional instability of sea water at the freezing point, *Deep*  
801 *Sea Res.*, **21**, 169–174, 1974.



- 802 Foldvik, A., Gammelsrød, T., Nygaard, E. and Østerhus, S.: Current meter measurements  
803 near Ronne Ice Shelf, Weddell Sea: Implications for circulation and melting underneath  
804 the Filchner-Ronne ice shelves, *J. Geophys. Res.*, 106 (C3), 4463–4477, 2001.
- 805 Gagliardini, O., Durand, G., Zwinger, T., Hindmarsh, R. C. A. and Le Meur, E.: Coupling of  
806 ice shelf melting and buttressing is a key process in ice-sheet dynamics, *Geophys. Res.*  
807 *Lett.*, 37, L14501, doi:10.1029/2010GL043334, 2010.
- 808 Gammelsrød, T., et al.: Distribution of water masses on the continental shelf in the southern  
809 Weddell Sea, in *Polar oceans and their role in shaping the global environment*, edited by  
810 M. Johannessen, R. D. Muench, and J. E. Overland, pp. 159–175, American Geophysical  
811 Union, Washington, D. C., 1994.
- 812 Gerdes, R., Determann, J., and Grosfeld, K.: Ocean circulation beneath Filchner-Ronne Ice  
813 Shelf from three-dimensional model results, *J. Geophys. Res.*, 104 (C7), 15,827–15,842,  
814 1999.
- 815 Groh, A., and Horwath, M.: The method of tailored sensitivity kernels for GRACE mass  
816 change estimates. *Geophys. Res. Abstr.*, 18, EGU2016-12065, 2016.
- 817 Haney, R. L.: On the pressure-gradient force over steep topography in sigma coordinate  
818 ocean models, *J. Phys. Oceanogr.*, 21(4) 610–619, 1991.
- 819 Harig, C., and Simons, F. J.: Accelerated West Antarctic ice mass loss continues to outpace  
820 East Antarctic gains, *Earth Planet. Sci. Lett.*, 415, 134–141, 2015.
- 821 Hellmer, H. H., and Olbers, D. J.: A two-dimensional model for the thermohaline circulation  
822 under an ice shelf, *Antarct. Sci.*, 1 (4), 325–336, 1989.
- 823 Hellmer, H. H.: Impact of antarctic ice shelf basal melting on sea ice and deep ocean  
824 properties, *Geophys. Res. Lett.*, 31 (10), L10307, doi:0094-8276/04/2004GL019506,  
825 2004.
- 826 Hellmer, H. H., Kauker, F., Timmermann, R., and Hattermann, T.: The fate of the southern  
827 Weddell Sea continental shelf in a warming climate, *J. Climate*, 2017.



- 828 Hellmer, H. H., Kauker, F., Timmermann, R., Determann, J., and Rae, J.: Twentyfirst-  
829 century warming of a large Antarctic ice-shelf cavity by a redirected coastal current,  
830 Nature, 485, 225–228, doi:10.1038/nature11064, 2012.
- 831 Holland, D. M., and Jenkins, A.: Modeling thermodynamic ice-ocean interactions at the base  
832 of an ice shelf, J. Phys. Oceanogr., 29 (8), 1787–1800, 1999.
- 833 Jacobs, S. S., Helmer, H. H., Doake, C. S. M., Jenkins, A. and Frolich, R. M.: Melting of ice  
834 shelves and the mass balance of Antarctica, J. Glaciol., 38(130), 375–387, 1992.
- 835 Jenkins, A.: A one-dimensional model of ice shelf-ocean interaction, J. Geophys. Res.-  
836 Ocean., 96(C11), 20,671–20,677, 1991.
- 837 Jenkins, A., Hellmer, H.H., and Holland, D.M.: The role of meltwater advection in the  
838 formulation of conservative boundary conditions at an ice-ocean interface, J. Phys.  
839 Oceanogr., 31, 285–296, 2001.
- 840 Jenkins, A., Nicholls, K. W., and Corr, H. F. J.: Observations and parameterization of  
841 ablation at the base of Ronne Ice Shelf, Antarctica, J. Phys. Oceanogr., 40, 2298–2312,  
842 2010.
- 843 Joughin, I. and Padman, L.: Melting and freezing beneath Filchner-Ronne Ice Shelf,  
844 Antarctica, Geophys. Res. Lett., 30 (9), 1477, doi:10.1029/2003GL016941, 2003.
- 845 Joughin, I., Smith, B. E., and Medley, B.: Marine ice sheet collapse potentially under way  
846 for the Thwaites Glacier basin, West Antarctica, Science, 344, 735–738, 2014.
- 847 Khazendar, A., Rignot, E., Schroeder, D.M., Seroussi, H., Schodlok, M.P., Scheuchl, B.,  
848 Mouginot, J., Sutterley, T.C. and Velicogna, I.: Rapid submarine ice melting in the  
849 grounding zones of ice shelves in West Antarctica. Nat. Commun., 7, 2016.
- 850 Kobs, S., Holland, D. M., Zagorodnov, V., Stern, A. and Tyler, S. W.: Novel monitoring of  
851 Antarctic ice shelf basal melting using a fiber-optic distributed temperature sensing  
852 mooring. Geophys. Res. Lett., 41(19), 6779–6786, 2014.



- 853 Makinson, K., and K. Nicholls: Modeling Tidal currents beneath Filchner-Ronne Ice Shelf  
854 and on the adjacent continental shelf: Their effect on mixing and transport, *J. Geophys.*  
855 *Res.*, 104(C6), 13,449–13,465, 1999.
- 856 Makinson, K., Schröder, M., and Østerhus, S.: Effect of critical latitude and seasonal  
857 stratification on tidal current profiles along Ronne Ice Front, Antarctica, *J. Geophys. Res.-*  
858 *Ocean.*, 111(C3), C03022, doi:10.1029/2005JC003062, 2006.
- 859 Makinson, K., Holland, P., Jenkins, A., Nicholls, K. W., and Holland, D. M.: Influence of  
860 tides on melting and freezing beneath Filchner-Ronne Ice Shelf, Antarctica, *Geophys.*  
861 *Res. Lett.*, 38, L06601, doi:10.1029/2010GL046462, 2011.
- 862 Marchesiello, P., McWilliams, J. C., Shchepetkin, A.: Open boundary conditions for long-  
863 term integration of regional oceanic models, *Ocean Modeling*, 3(1–2), 1–20, 2001.
- 864 Martin, M. A., Levermann, A., and Winkelmann, R.: Comparing ice discharge through West  
865 Antarctic Gateways: Weddell vs. Amundsen Sea warming, *Cryosphere Discuss.*, 9,  
866 1705–1733, 2015.
- 867 McPhee, M. G., Morison, J. H., and Nilsen, F.: Revisiting heat and salt exchange at the ice-  
868 ocean interface: Ocean flux and modeling considerations, *J. Geophys. Res.-Ocean.*, 113,  
869 C06014, doi:10.1029/2007JC004383, 2008.
- 870 Mengel, M., Feldmann, J., Levermann, A.: Linear sea-level response to abrupt ocean  
871 warming of major West Antarctic ice basin, *Nat. Clim. Change*, 6, 71–74,  
872 doi:10.1038/nclimate2808, 2016.
- 873 Mercer, J.H.: West Antarctic ice sheet and CO<sub>2</sub> greenhouse effect: a threat of disaster,  
874 *Nature*, 271, 321–325, 1978.
- 875 Moholdt, G., Padman, L., and Fricker, A.: Basal mass budget of Ross and Filchner-Ronne  
876 ice shelves, Antarctica, derived from Lagrangian analysis of ICESat altimetry. *J.*  
877 *Geophys. Res.-Earth Surf.*, 119(11), 2361–2380, 2014.



- 878 Monaghan, A. J., Bromwich, D. H., Fogt, R. L., Wang, S. H., Mayewski, P. A., Dixon, D.  
879 A., Ekaykin, A., Frezzotti, M., Goodwin, I., Isaksson, E. and Kaspari, S. D.: Insignificant  
880 change in Antarctic snowfall since the International Geophysical Year, *Science*,  
881 313(5788), 827–831, 2006.
- 882 Mougnot, J., Rignot, E., and Scheuchl, B.: Sustained increase in ice discharge from the  
883 Amundsen Sea Embayment, West Antarctica, from 1973 to 2013, *Geophys. Res. Lett.*,  
884 41, doi:10.1002/2013GL059069, 2014.
- 885 Mueller, R. D., Padman, L., Dinniman, M. S., Erofeeva, S. Y., Fricker, H. A., and King, M.  
886 A.: Impact of tide-topography interactions on basal melting of Larsen C Ice Shelf,  
887 Antarctica, *J. Geophys. Res.*, 117, C05005, doi:10.1029/2011JC007263, 2012.
- 888 Mueller, R.D.: The effects of thermodynamic parameterizations, ice shelf geometry, and  
889 tides on modeled basal melting of Weddell Sea ice shelves, doctoral dissertation, Oregon  
890 State University, <http://ir.library.oregonstate.edu/xmlui/handle/1957/49292>, 2014.
- 891 Nicholls, K. W., Østerhus, S., Makinson, K., and Johnson, M. R.: Oceanographic conditions  
892 south of Berkner Island, beneath Filchner-Ronne Ice Shelf, Antarctica, *J. Geophys. Res.-*  
893 *Ocean.*, 106 (C6), 11,481–11,492, 2001.
- 894 Nicholls, K. W., Padman, L., Schröder, M., Woodgate, R. A., Jenkins, A., and Østerhus, S.:  
895 Water Mass Modification Over the Continental Shelf North of Ronne Ice Shelf,  
896 Antarctica, *J. Geophys. Res.-Ocean.*, 108 (C8), 3260, 2003.
- 897 Nicholls, K. W., and Østerhus, S.: Interannual variability and ventilation timescales in the  
898 ocean cavity beneath Filchner-Ronne Ice Shelf, Antarctica, *J. Geophys. Res.*, 109,  
899 C04014, doi:10.1029/2003JC002149, 2004.
- 900 Nicholls, K. W., Østerhus, S., Makinson, K., and Gammelsrød, T., and Fahrbach, E.: Ice-  
901 ocean processes over the continental shelf of the southern Weddell Sea, Antarctica: A  
902 review, *Rev. Geophys.*, 47, RG3003, doi:8755-1209/09/2007RG000250, 2009.



- 903 Padman, L., Fricker, H. A., Coleman, R., Howard, S., and Erofeeva, S.: A new tidal model  
904 for the Antarctic ice shelves and seas, *J. Glaciol.*, **34**, 247–254, 2002.
- 905 Padman, L., Siegfried, M. R., and Fricker, H. A.: The role of ocean tides on Antarctic and  
906 Greenland ice-sheet processes, *Rev. Geophys.*, in review.
- 907 Paolo, F. S., Fricker, H. A. and Padman, L.: Volume loss from Antarctic ice shelves is  
908 accelerating, *Science* **348**, 327–331, 2015.
- 909 Paolo, F. S., Fricker, H. A., & Padman, L.: Constructing improved decadal records of  
910 Antarctic ice shelf height change from multiple satellite radar altimeters. *Remote Sens.*  
911 *Environ.*, **177**, 192–205, 2016.
- 912 Pritchard, H. D., Ligtenberg, S. R. M., Fricker, H. A., Vaughan, D. G., van den Broeke, M.  
913 R., and Padman, L.: Antarctic ice-sheet loss driven by basal melting of ice shelves,  
914 *Nature*, **484**, 502–505, doi: 10.1038/nature10968, 2012.
- 915 Raymond, W. H. and H. L. Kuo: A radiation boundary condition for multi-dimensional  
916 flows, *Quart. J. R. Met. Soc.*, **110**, 535–551, 1984.
- 917 Rignot, E., and Jacobs, S. S.: Rapid bottom melting widespread near Antarctic Ice Sheet  
918 grounding lines, *Science*, **296** (5575), 2020–2023, doi:10.1126/science.1070942, 2002.
- 919 Rignot, E., Mouginot, J., and Scheuchl, B.: Ice-shelf melting around Antarctica, *Science*,  
920 **341**(6143), 266–270, doi:10.1126/science.1235798, 2013.
- 921 Rignot, E., Mouginot, J., Morlighem, M., Seroussi, H. and Scheuchl, B.: Widespread, rapid  
922 grounding line retreat of Pine Island, Thwaites, Smith, and Kohler glaciers, West  
923 Antarctica, from 1992 to 2011. *Geophys. Res. Lett.* **41**, 3502–3509, 2014.
- 924 Robertson, R., Padman, L., and Egbert, G.: Tides in the Weddell Sea, in *Oceanology of the*  
925 *Antarctic Continental Shelf*, *Antarct. Res. Ser.*, vol. 75, edited by S. Jacobs and R.  
926 Weiss, pp. 341–369, AGU, Washington, D. C., 1998.



- 927 Rosier, S. H. R., Green, J. A. M., Scourse, J. D., and Winkelmann, R.: Modeling Antarctic  
928 tides in response to ice shelf thinning and retreat, *J. Geophys. Res. Oceans*, 119(1), 87-  
929 97, 2014.
- 930 Ross, N., Bingham, R. G., Corr, H. F., Ferraccioli, F., Jordan, T. A., Le Brocq, A., Rippin,  
931 D. M., Young, D., Blankenship, D. D., and Siegert, M.J.: Steep reverse bed slope at the  
932 grounding line of the Weddell Sea sector in West Antarctica, *Nat. Geo.*, 5(6), 393–396,  
933 2012.
- 934 Scambos, T. A., Bohlander, J. A., Shuman, C. A., and Skvarca, P.: Glacier acceleration and  
935 thinning after ice shelf collapse in the Larsen B embayment, Antarctica, *Geophys. Res.*  
936 *Lett.*, 31, L18402, doi:10.1029/2004GL020670, 2004.
- 937 Schlosser, P., Bayer, R., Foldvik, A., Gammelsrød, T., Rohardt, G., Münnich, K. O.: Oxygen  
938 18 and Helium as tracers of ice shelf water and water/ice interactions in the Weddell Sea,  
939 *J. of Geophys. Res.*, 95 (C3), 3253–3263, 1990.
- 940 Schodlok, M. P., Menemenlis, D., Rignot, E. and Studinger, M.: Sensitivity of the ice-  
941 shelf/ocean system to the sub-ice-shelf cavity shape measured by NASA IceBridge in  
942 Pine Island Glacier, West Antarctica. *Annals of Glaciology*, 53(60), pp.156-162, 2012.
- 943 Schoof, C.: Ice sheet grounding line dynamics: Steady states, stability, and hysteresis. *J. of*  
944 *Geophys. Res.: Earth Surface*, 112(F3), 2007.
- 945 Shchepetkin, A. F., and McWilliams, J. C.: A method for computing horizontal pressure-  
946 gradient force in an oceanic model with a nonaligned vertical coordinate, *J. Geophys.*  
947 *Res.-Ocean.*, 108(C3), doi:10.1029/2001JC001047, 2003.
- 948 Shchepetkin, A. F., and McWilliams, J. C.: Correction and commentary for “Ocean  
949 forecasting in terrain-following coordinates: Formulation and skill assessment of the  
950 regional ocean modeling system” by Haidvogel et al., *J. Comp. Phys.* 227, pp. 3595–  
951 3624, *J. Comp. Phys.*, 228(24), 8985–9000, doi:10.1016/j.jcp.2009.09.002, 2009.



- 952 Shepherd et al.: A Reconciled Estimate of Ice-Sheet Mass Balance, *Science*, 338, 1183-  
953 1189, doi: 10.1126/science.1228102, 2012.
- 954 Sutterley, T. C., Velicogna, I., Rignot, E., Mouginot, J., Flament, T., van den Broeke, M. R.,  
955 van Wessem, J. M., and Reijmer, C. H.: Mass loss of the Amundsen Sea Embayment of  
956 West Antarctica from four independent techniques, *Geophys. Res. Lett.*, 41, 8421–8428,  
957 doi:10.1002/2014GL061940, 2014.
- 958 Timmermann, R., et al.: A consistent dataset of Antarctic ice sheet topography, cavity  
959 geometry, and global bathymetry, *Earth System Science Data*, 2, 261–273,  
960 doi:10.5194/essd-2-261-2010, 2010.
- 961 Timmermann, R., Wang, Q., and Hellmer, H. H.: Ice-shelf basal melting in a global finite-  
962 element sea-ice/ice-shelf/ocean model, *Ann. Glaciol.*, 53 (60), 303–314,  
963 doi:10.3189/2012AoG60A156, 2012.
- 964 Timmermann, R. and Hellmer, H. (2013): Southern Ocean warming and increased ice shelf  
965 basal melting in the twenty-first and twenty-second centuries based on coupled ice-ocean  
966 finite-element modelling, *Ocean Dynamics*, 63 (9), pp. 1011–1026. doi:  
967 10.1007/s10236-013-0642-0.
- 968 Walker, R. T., Dupont, T. K., Parizek, B. R., and Alley, R. B.: Effects of basal-melting  
969 distribution on the retreat of ice-shelf grounding lines, *Geophys. Res. Lett.*, 35, L17503,  
970 doi:10.1029/2008GL034947, 2008.
- 971 Webber, B. G. M, Heywood, K. J., Stevens, D. P., Dutrieux, P., Abrahamsen, E. P., Jenkins,  
972 A., Jacobs, S. S., Ha, H. K., Lee, S. H., Kim, T. W., Mechanisms driving variability in  
973 the ocean forcing of Pine Island Glacier, *Nat. Commun.*, 8, 14507,  
974 doi:10.1038/ncomms14507, 2017.
- 975 Wright, A. P., Le Brocq, A. M., Cornford, S., Bingham, R. G., Corr, H. F. J., Ferraccioli, F.,  
976 Jordan, T. A., Payne, A. J., Rippin, D. M., Ross, N. and Siegert, M. J.: Sensitivity of the



977 Weddell Sea sector ice streams to sub-shelf melting and surface accumulation, The  
978 Cryosphere, 8, 2119–2134, doi:10.5194/tc-8-2119-2014, 2014.



979  
 980  
 981  
 982  
 983

**Table 1** An overview of the eight model runs presented in this paper and the case name that is used to reference them. The three runs that were used as the spin-up solutions to initialize other runs are marked and referenced as b1, b2, and b3. The four runs that include passive dye tracers are shaded in grey. All run intervals provide steady state solutions as determined by the transient solutions of shelf-averaged basal melt.

#	Case Name	Run length	Averaged output period	Cavity geometry	$\theta_{init}$ (°C)	min $z_{ice}$ (m)	max $z_{ice}$ (m)	min $wct$ (m)	max $wct$ (m)
1	standard cold tide-forced	20-years	30-day	present-day	-1.9	-11	-1537	50	1210
2	standard cold no-tides	10-years	30-day	present-day	-1.9	''	''	''	''
3	standard warm tide-forced	20-years	30-day	present-day	-1.4	''	''	''	''
4	standard warm no-tides	10-years	30-day	present-day	-1.4	''	''	''	''
5	standard tides-only	30-days	2-hour	present-day	NA	''	''	''	''
6	standard cold dye (restart #1)	2-year	30-day	present-day	-1.9	''	''	''	''
8	standard warm dye (restart #3)	2-year	30-day	present-day	-1.4	''	''	''	''
9	modified warm tide-forced	20-year	30-day	melt-adjusted	-1.4	-25	-1442	52	1180
10	modified warm no-tides	10-year	30-day	melt-adjusted	-1.4	''	''	''	''
11	modified tides-only	30-days	2-hour	melt-adjusted	NA	''	''	''	''
12	modified warm dye (restart #9)	2-year	30-day	melt-adjusted	-1.4	''	''	''	''



984

985 **Table 2** Values for integrated mass transport ( $M_b$ ,  $\text{Gt a}^{-1}$ ) and FRIS-averaged basal melt rate ( $w_b$ ,  $\text{m a}^{-1}$ ) for the six  
986 runs shown in Fig. 6: Standard cold no-tides (S -1.9 ☉), Standard cold tides-forced (S -1.9), Standard warm no-tides  
987 (S -1.4 ☉), Standard warm tides-forced (S -1.4), Modified warm no-tides (M -1.4 ☉), Modified warm tides-forced  
988 (M -1.4).

		S -1.9 ☉	S -1.9	S -1.4 ☉	S -1.4	M -1.4 ☉	M -1.4
$M_b$ ( $\text{Gt a}^{-1}$ )	Net	48	47	171	239	188	221
	Melt	62	104	182	262	200	246
	Freeze	-14	-57	-11	-23	-12	-25
$w_b$ ( $\text{ma}^{-1}$ )	Net	0.14	0.14	0.49	0.69	0.54	0.63
	Melt	0.27	0.46	0.66	0.95	0.69	0.86
	Freeze	-0.12	-0.44	-0.14	-0.29	-0.20	-0.37

989



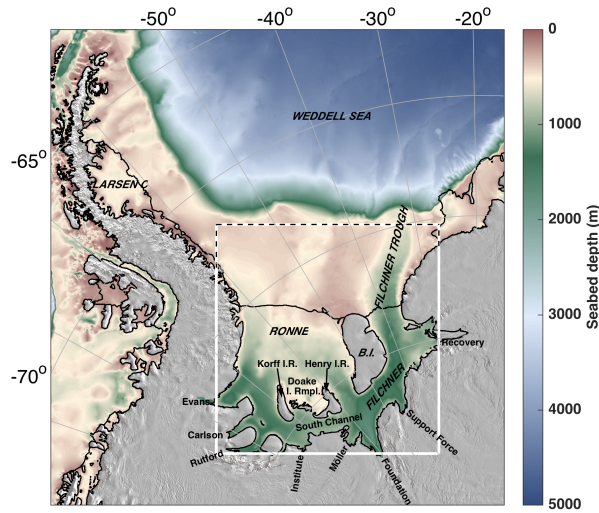
990  
 991 **Table 3** Publication sources and abbreviations used in Fig. 3. Method of calculating melt rates is summarized as Ocean Model (OM), Standard Glaciological Method  
 992 (GM), Ocean Observation (OO), Geophysical Tracer (GT), following the nomenclature used in Table S2 of Rignot et al. (2013) supplementary document. The time  
 993 period of observation(s) or forcing files are listed together with source of data or model output.

Pub. Abbr.	method	reference	time period	estimate source
TS	OM	this study	NA	numerical model
M14	GM	Moholdt et al. (2014)	2003-2009	
R13	GM	Rignot et al. (2013)	2003-2009	ICESat
			2007-2008	ALOS PALSAR
				InSAR
			1979-2010	RACMO2
				Operation IceBridge
				BEDMAP
D13	GM	Depoorter et al. (2013)	2003-2009	ICESat
			1994-2002	ERS-1
			2007-2009	ERS-2
			2007-2009	InSAR
			1979-2010	RACMO2
T12	OM	Timmermann et al. (2012)	1958-2010	FESOM model, NCEP winds (1958-2010)
M11	OM	Makinson et al. (2011)	NA	
H04	OM	Hellmer (2004)	1978-1997	NCEP 10-m winds



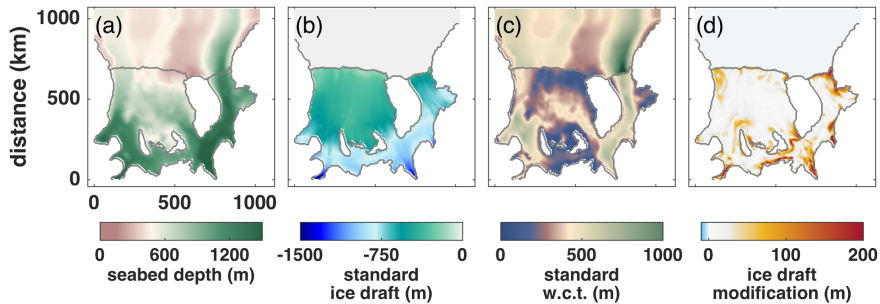
					2-m air temperature
					specific humidity
					cloudiness
					and net precipitation
JP03	GM	Joughin and Padman (2003)	1997		RADARSAT InSAR
N03	OO	Nicholls et al. (2003)	1995-1999		CTD
F01	OO	Foldvik et al. (2001)	1992-1993		CTD & mooring
G99	OM	Gerdes et al. (1999)	NA		
G94	GT	Gammelstrød et al. (1994)	Feb. 1993		CFC-11, CFC-12, O <sub>2</sub> , Si
J92	GM	Jacobs et al. (1992)			
JD91	GM	Jenkins (1991)	1985-1988		Radar echo sounding
S90	GT	Schlosser et al. (1990)	Jan-Mar. 1985		$\delta_{18}\text{O}$ , He

994  
 995



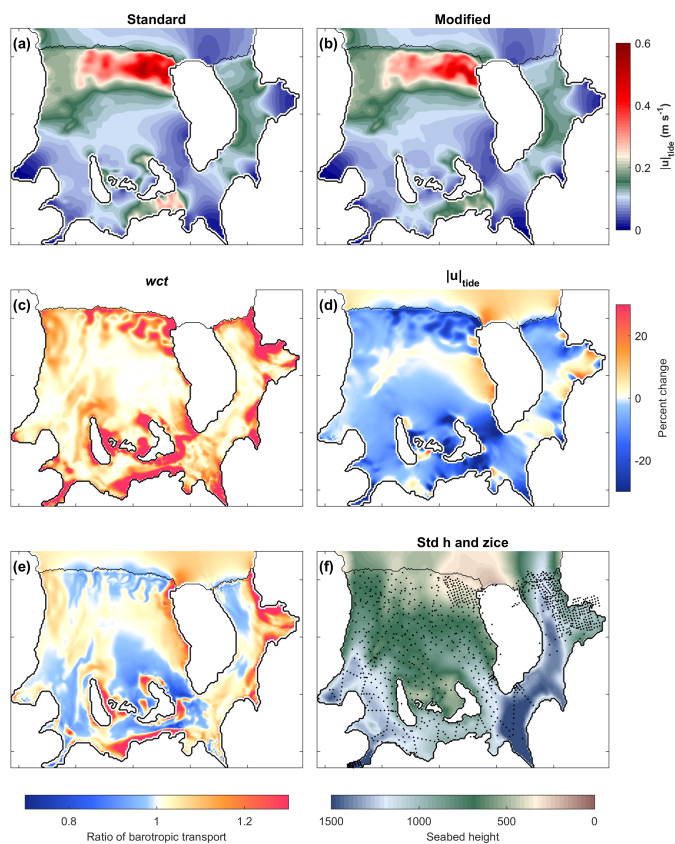
997

998 Figure 1: Weddell Sea region of study with model domain outlined by white box. Dashed black lines highlight the  
 999 open boundaries. The labels on land indicate the names of the tributary glaciers used for regional analyses in this  
 1000 study. Black lines over seabed indicate the extend of th ice shelf and black lines around the grey mask indicate the  
 1001 ice sheet grounding line and/or transition between ocean and land.



1002

1003 Figure 2: Bathymetry ( $h$ ) and ice draft ( $z_{ice}$ ) for the standard and modified geometries: (a)  $h$  for both the standard  
 1004 and modified cases; (b)  $z_{ice}$  for the standard case; (c)  $w.c.t.$  for the standard case; (d) Difference between standard  $z_{ice}$   
 1005 and modified  $z_{ice}$ , where difference  $> 0$  indicates regions of melting and a corresponding decrease in  $z_{ice}$  in the  
 1006 modified geometry when compared to the standard geometry.



1007

1008

1009

1010

1011

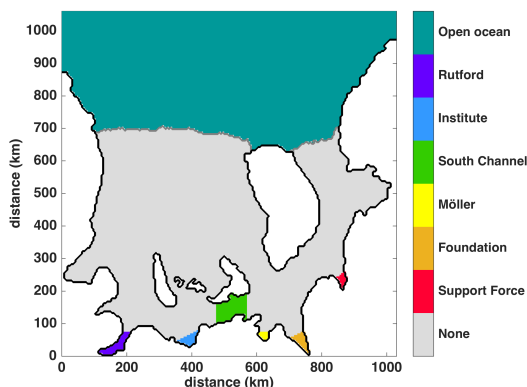
1012

1013

1014

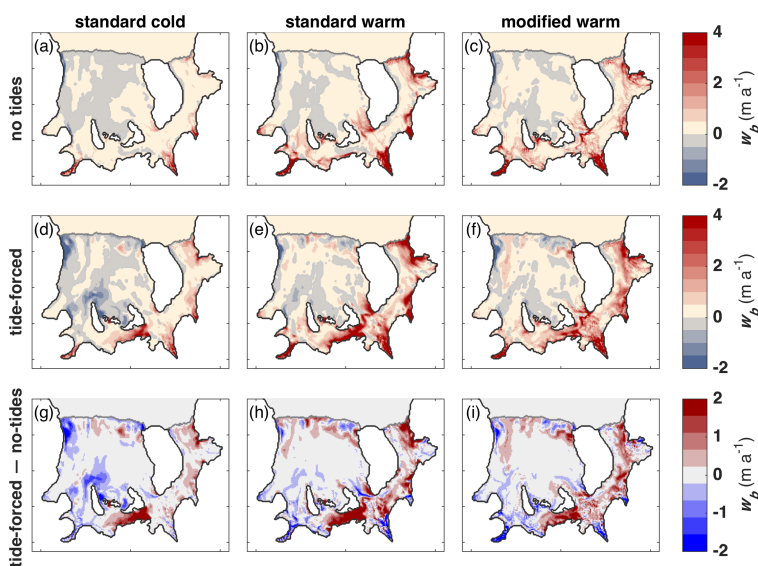
Figure 3: (a) Barotropic current ( $|u|_{tides}$ , Eqn. (5)) for the standard tides-only run. (b) Same as (a) but for the modified tides-only run. (c) Percent change in  $wct$  between the standard and modified cases with positive values indicating where the  $wct$  is greater in the modified geometry than the standard geometry. (d) Change in  $|u|_{tide}$  between (a) and (b) where Percent change  $> 0$  indicates locations where the standard case  $|u|_{tide}$  is greater than the modified case  $|u|_{tide}$ . (e) Ratio of barotropic transport ( $wct \times |u|_{tide}$ ) shown here as modified/standard, with values  $> 0$  showing where there is increased transport for the modified case. (f) Seabed depth (as in Figure 2a) with existing seismic observation locations shown as black dots.

1015



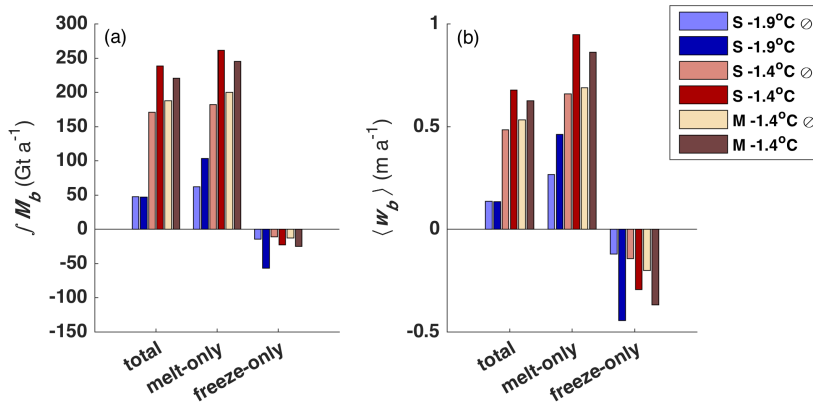
1016  
 1017

Figure 4: Locations of the six meltwater dyes and the open ocean bulk dye explained in Sec. 2.3.3.



1018  
 1019  
 1020  
 1021  
 1022  
 1023

Figure 5: Melt rates averaged over 1-year of steady state solutions for (top) no tides runs, (middle) tide-forced runs, and (bottom) the difference between the tide-forced and no-tides melt solutions. Positive values in the bottom subplots show where there is more basal melting in the solutions that include tidal forcing (middle subplots). The left column (a, d, g) shows results for the standard cold case; the middle column (b, e, h) shows results for the standard warm case; and the right column (c, f, i) shows results for the modified warm case.

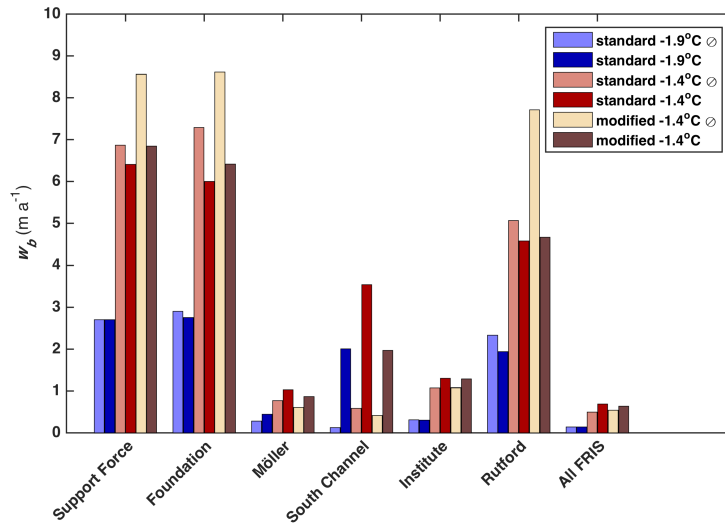


1024

1025

1026

Figure 6: (a) integrated mass flux over “total” FRIS area, “melt-only” regions, and “freeze-only” regions for both no-tide (⊙) and tide-forced cases. (b) Same regions and runs as in (a) but showing FRIS-averaged basal melting.



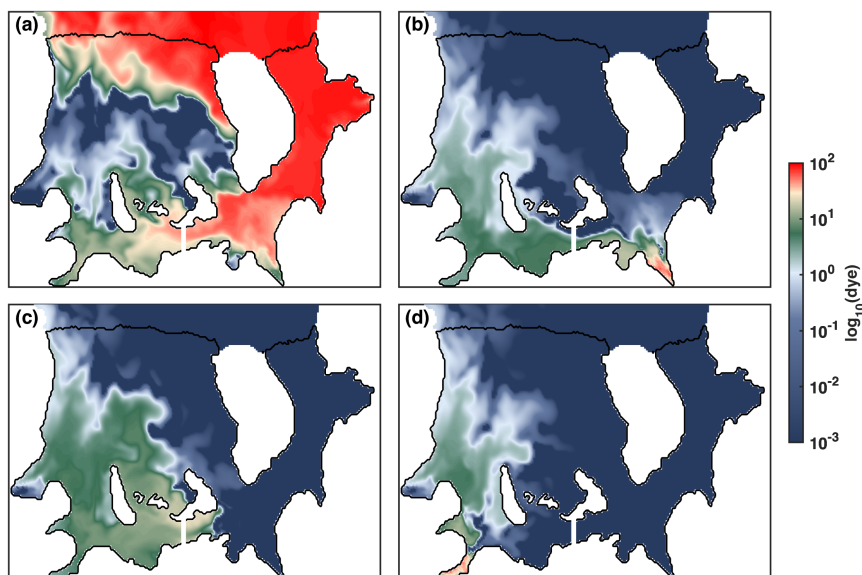
1027

1028

1029

1030

Figure 7: Melt rates averaged over last 12 months of steady state solutions in the standard cold, standard warm, and modified warm cases for some of the regions shown in Fig. 4 and for both no-tides (⊙) and tide-forced simulations. “All FRIS” duplicates the information shown by “total” in Fig. 6b.



1031

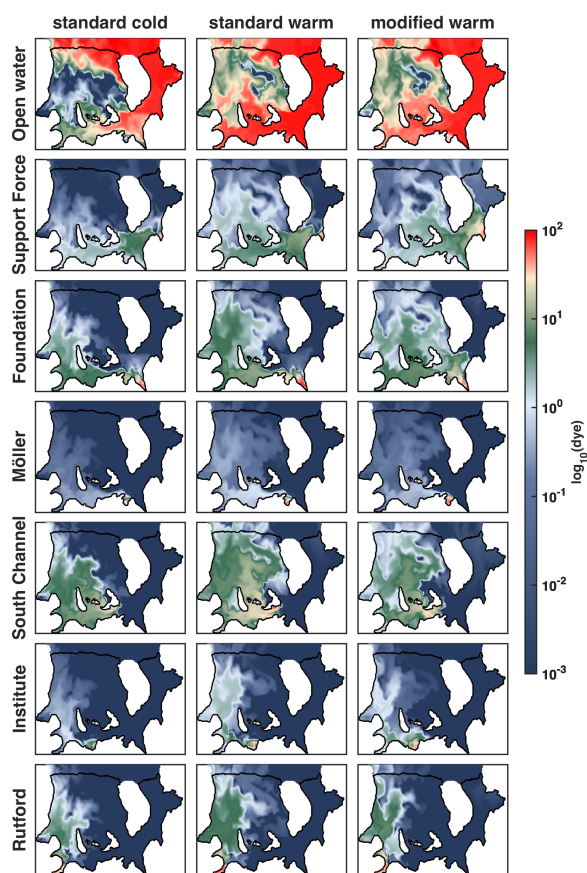
1032

1033

1034

1035

**Figure 8:** Distribution of dye concentration from the last time step and the upper model layer of the standard cold, tide-forced case described in Sect. 2.3.3. (a) bulk dye representing penetration of water initially north of the FRIS ice front. (b-d) meltwater dyes with sources in Foundation inlet, South Channel, and Rutford inlet, respectively (see Fig. 4 for dye release locations). The white line across South Channel represents the location of the transects in Fig. 13.



1036

1037

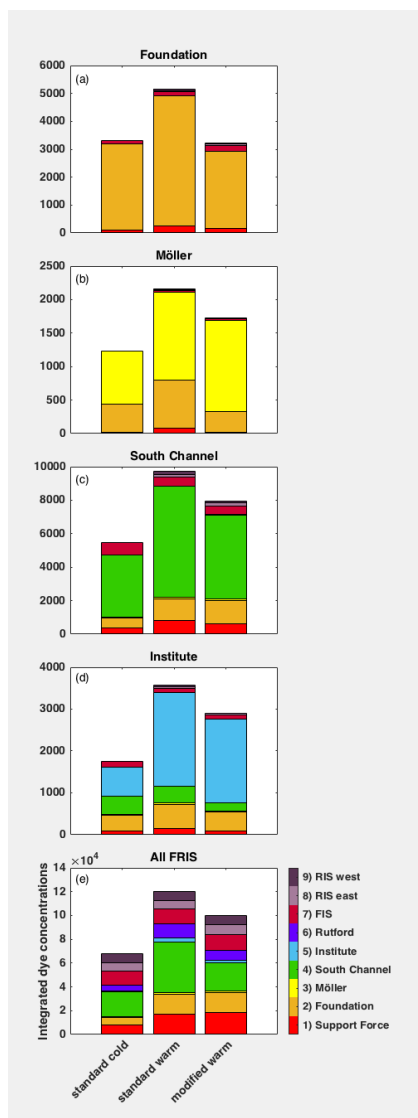
1038

1039

1040

Figure 9: An expanded distribution of dye concentration than that shown in Fig. 8 to include all meltwater dyes in the three tide-forced base simulations. As in Fig. 8, dye concentrations are from the last 30-day average of upper model layer solutions from the runs described in Sect. 2.3.3. The left hand column of this graphic includes the same four regional plots as shown in Fig. 8.

1041



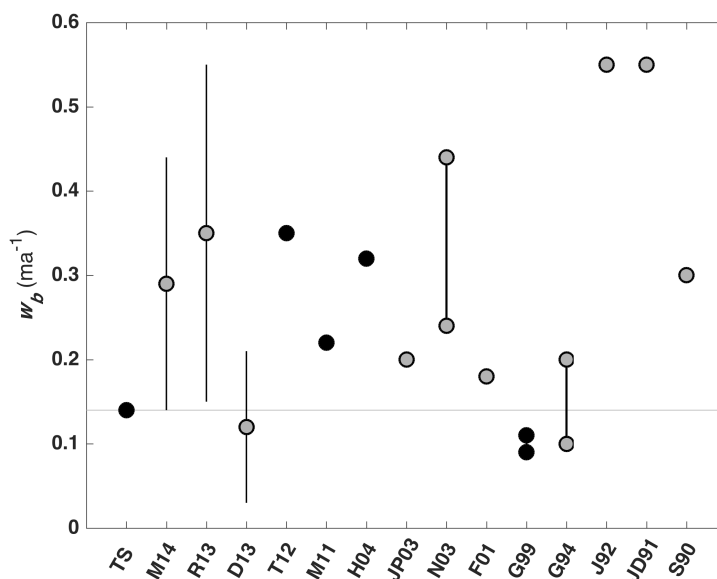
1042

1043

1044

1045

Figure 10 Integrated meltwater dye (Sect. 2.3.3) by region for the tide-forced, base simulations, showing: (a) Foundation region, (b) Möller region, (c) South Channel region, (d) Institute region, and (e) all of FRIS. Regions are defined in Fig. 4.



1046

1047

1048

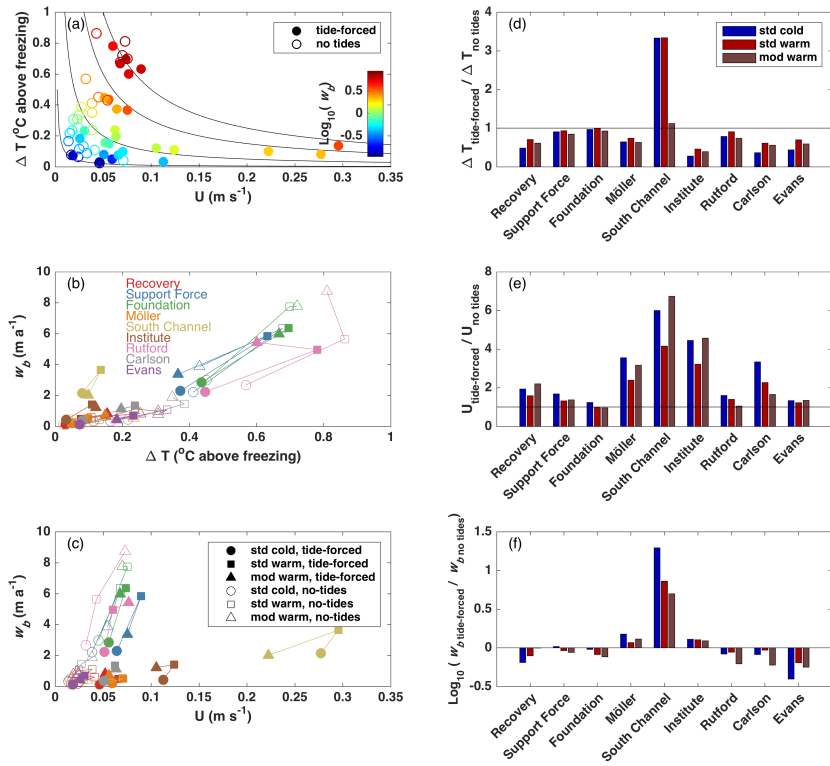
1049

1050

1051

1052

Figure 11 FRIS-averaged basal melt rate comparison between this study [TS] and others. Model results are shown as black dots while observations are shown as grey dots. Error bars for remote sensing observations are shown as black lines for M14 (Moholdt et al., 2014), R13 (Rignot et al., 2013) and D13 (Depoorter et al., 2013). Min and max values are connected by thick, solid, black lines to show the range of values reported by N03 (Nicholls et al., 2003) and G94 (Gammelsrød et al., 1994). A summary of the studies presented here and their abbreviations is provided in Table 2.



1053

1054

1055

1056

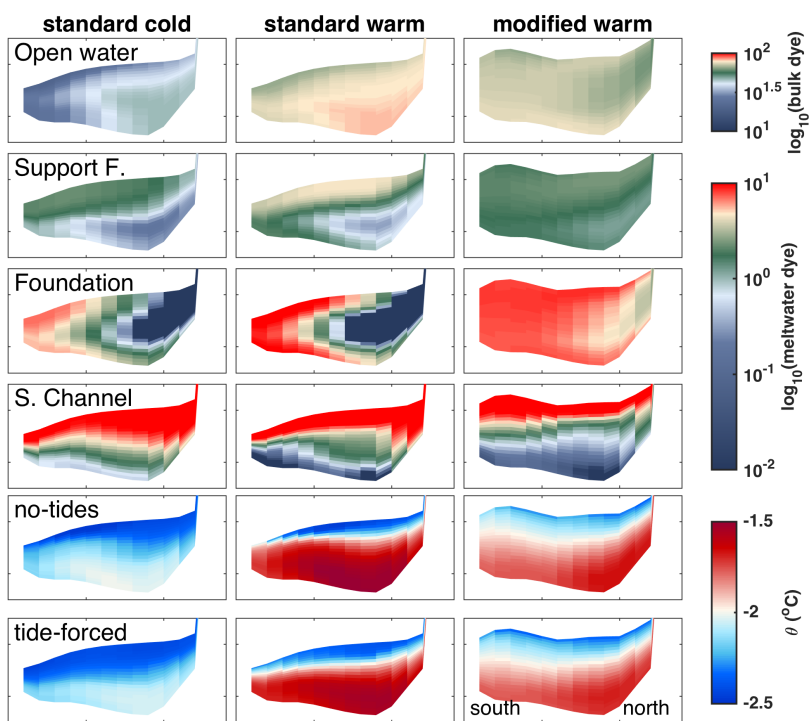
1057

1058

1059

1060

Figure 12: Regional influences of  $\Delta T$  and current speed on melt rates. Tide-forced cases are plotted using solid marker style, e.g. “■”, and no-tide cases are plotted using open marker style, e.g. “□”. (a) Current speed ( $U$ , Eqn. (6)) vs. thermal forcing ( $\Delta T$ ), color-coded according to melt rate ( $w_b$ ). Black contours follow  $\Delta T = c/U$  (with  $c$  being a set of different scalars), along which constant values of  $w_b$  (as in Sect. 2.3.1) are expected to be found. (b)  $\Delta T$  vs.  $w_b$  for each region. (c)  $U$  vs.  $w_b$  for each region. (d)  $\Delta T$  difference between no-tides and tide-forced cases such that positive values show where thermal forcing is stronger in the no-tides cases, (e) current speed difference between tide-forced ( $U_{\text{tides}}$ ) and no-tides ( $U_{\text{no tides}}$ ) cases, and (f)  $w_b$  difference between tide-forced and no-tides cases.



1061  
 1062  
 1063  
 1064

Figure 13: Transects of dyes (upper four rows) and potential temperature ( $\theta$ , lower two panels) across South Channel at the western tip of Henry Ice Rise. The upper four panels are for tide-forced runs only. Transect location is shown in Fig. 8.